

Special Section:

Understanding carbon-climate feedbacks

Key Points:

- Consistent flux constraints are provided by surface in situ and flask, TCCON, and GOSAT measurements of atmospheric CO₂
- Combining data sets improves agreement between modeled and measured aircraft-based CO₂ measurements
- Improvements in NASA ACOS retrieval explain improved consistency of space-based and surface-based CO₂

Supporting Information:

- Supporting Information S1

Correspondence to:

B. Byrne,
brendan.k.byrne@jpl.nasa.gov

Citation:






















Byrne, B., Liu, J., Lee, M., Baker, I., Bowman, K. W., Deutscher, N. M., et al. (2020). Improved constraints on northern extratropical CO₂ fluxes obtained by combining surface-based and space-based atmospheric CO₂ measurements. *Journal of Geophysical Research: Atmospheres*, 125, e2019JD032029. <https://doi.org/10.1029/2019JD032029>

Received 8 NOV 2019

Accepted 13 JUN 2020

Accepted article online 24 JUN 2020

Improved Constraints on Northern Extratropical CO₂ Fluxes Obtained by Combining Surface-Based and Space-Based Atmospheric CO₂ Measurements

B. Byrne¹ , J. Liu^{1,2} , M. Lee¹ , I. Baker³ , K. W. Bowman¹ , N. M. Deutscher⁴ , D. G. Feist^{5,6,7} , D. W. T. Griffith⁴ , L. T. Iraci⁸ , M. Kiel¹ , J. S. Kimball⁹ , C. E. Miller¹ , I. Morino¹⁰ , N. C. Parazoo¹ , C. Petri¹¹ , C. M. Roehl² , M. K. Sha¹² , K. Strong¹³ , V. A. Velazco⁴ , P. O. Wennberg^{2,14} , and D. Wunch¹³ 

¹Jet Propulsion Laboratory, California Institute of Technology, Pasadena, CA, USA, ²Division of Geological and Planetary Sciences, California Institute of Technology, Pasadena, CA, USA, ³Atmospheric Science Department, Colorado State University, Fort Collins, CO, USA, ⁴Centre for Atmospheric Chemistry, School of Earth, Atmospheric and Life Sciences, University of Wollongong, Wollongong, New South Wales, Australia, ⁵Max Planck Institute for Biogeochemistry, Jena, Germany, ⁶Lehrstuhl für Physik der Atmosphäre, Ludwig-Maximilians-Universität München, Munich, Germany, ⁷Institut für Physik der Atmosphäre, Deutsches Zentrum für Luft- und Raumfahrt, Oberpfaffenhofen, Weßling, Germany, ⁸Atmospheric Science Branch, NASA Ames Research Center, Moffett Field, CA, USA, ⁹Numerical Terradynamic Simulation Group, W.A. Franke College of Forestry & Conservation, The University of Montana, Missoula, MT, USA, ¹⁰Satellite Observation Center, Center for Global Environmental Research, National Institute for Environmental Studies (NIES), Tsukuba, Japan, ¹¹Institute of Environmental Physics, University of Bremen, Bremen, Germany, ¹²Royal Belgian Institute for Space Aeronomy (BIRA-IASB), Brussels, Belgium, ¹³Department of Physics, University of Toronto, Toronto, Ontario, Canada, ¹⁴Division of Engineering and Applied Science, California Institute of Technology, Pasadena, CA, USA

Abstract Top-down estimates of CO₂ fluxes are typically constrained by either surface-based or space-based CO₂ observations. Both of these measurement types have spatial and temporal gaps in observational coverage that can lead to differences in inferred fluxes. Assimilating both surface-based and space-based measurements concurrently in a flux inversion framework improves observational coverage and reduces sampling related artifacts. This study examines the consistency of flux constraints provided by these different observations and the potential to combine them by performing a series of 6-year (2010–2015) CO₂ flux inversions. Flux inversions are performed assimilating surface-based measurements from the in situ and flask network, measurements from the Total Carbon Column Observing Network (TCCON), and space-based measurements from the Greenhouse Gases Observing Satellite (GOSAT), or all three data sets combined. Combining the data sets results in more precise flux estimates for subcontinental regions relative to any of the data sets alone. Combining the data sets also improves the accuracy of the posterior fluxes, based on reduced root-mean-square differences between posterior flux-simulated CO₂ and aircraft-based CO₂ over midlatitude regions (0.33–0.56 ppm) in comparison to GOSAT (0.37–0.61 ppm), TCCON (0.50–0.68 ppm), or in situ and flask measurements (0.46–0.56 ppm) alone. These results suggest that surface-based and GOSAT measurements give complementary constraints on CO₂ fluxes in the northern extratropics and can be combined in flux inversions to improve constraints on regional fluxes. This stands in contrast with many earlier attempts to combine these data sets and suggests that improvements in the NASA Atmospheric CO₂ Observations from Space (ACOS) retrieval algorithm have significantly improved the consistency of space-based and surface-based flux constraints.

1. Introduction

Observations of atmospheric CO₂ provide a constraint on the net surface-atmosphere CO₂ flux and are critical for monitoring carbon flux changes. This has motivated observational programs that measure atmospheric CO₂, including a global network of surface-based in situ and flask monitoring sites, the Total Carbon Column Observing Network (TCCON) of ground-based spectrometers (Wunch et al., 2011) and several satellite missions (Crisp et al., 2004; Yokota et al., 2009). These observations have provided many insights into the terrestrial and ocean carbon cycle (Bacastow, 1976; Bolin & Keeling, 1963; Bowman et al., 2017; Chatterjee et al., 2017; Keeling, 1960; Keeling et al., 1996; Liu et al., 2017; Tans et al., 1989). However,

©2020. The Authors.

This is an open access article under the terms of the Creative Commons Attribution License, which permits use, distribution and reproduction in any medium, provided the original work is properly cited.

current measurement programs are unable to continuously monitor CO₂ with global coverage, resulting in observational gaps. These spatial and temporal gaps in observations of atmospheric CO₂ can introduce artifacts into NEE estimates, leading to difficulties in constraining carbon fluxes on regional scales (Basu et al., 2018; Byrne et al., 2017; Collatz et al., 2014).

Different observing systems have different gaps in the observational coverage. Space-based measurements retrieve atmospheric CO₂ from measurements of reflected sunlight. This results in highly seasonal observational coverage in extratropical regions. Seasonal differences in observational coverage are further exacerbated by challenging retrievals over snow (Nassar et al., 2014) and seasonal variations in cloud cover. In contrast, surface-based measurements of atmospheric CO₂ typically have comparatively uniform temporal coverage but heterogeneous spatial coverage. Surface measurement sites most densely cover the northern extratropics (particularly North America and Europe) but have sparse coverage elsewhere (Byrne et al., 2017).

In the northern extratropics, surface-based and space-based atmospheric CO₂ measurements provide complementary observational coverage in space and time. Yet few studies have attempted to combine surface-based and space-based atmospheric CO₂ measurements to obtain top-down constraints on fluxes across the northern latitudes. Nassar et al. (2011) combined surface flask CO₂ measurements with space-based measurements from the Tropospheric Emission Spectrometer (TES) in an inversion system and found improved constraints on CO₂ fluxes, particularly in the tropics. Chevallier et al. (2011) found consistency between the surface air sample-based and the TCCON-based inversions, suggesting that flux inversions combining both data sources could be performed. Maksyutov et al. (2013) performed a combined inversion of monthly mean-gridded Greenhouse Gases Observing Satellite (GOSAT) X_{CO₂} and GLOBALVIEW-CO₂, finding that posterior fluxes were in close agreement with fluxes from a GLOBALVIEW-CO₂-only flux inversion in regions that are well constrained by GLOBALVIEW-CO₂ sampling network but showed considerable differences in other regions. Houweling et al. (2015) performed a series of CO₂ flux inversions assimilating measurements from GOSAT and surface-based CO₂ measurements. They found that comparisons between posterior CO₂ fields and aircraft data did not show significant differences between inversions assimilating surface-based or space-based measurements and that the largest differences were driven by the inversion setup. However, they also found that the two data sets gave large differences in the spatial distribution of the CO₂ sink, with GOSAT flux inversions having increased uptake in the northern extratropics by ~1 PgC. When both data sets were combined, they found that the posterior fluxes did not recover the observed meridional gradient in CO₂ (which was also found for the GOSAT flux inversions), suggesting that the biases in retrieved GOSAT X_{CO₂} could be adversely impacting the results. Another study (Wang et al., 2018) assimilated both GOSAT measurements and surface-based atmospheric CO₂ measurements in a batch Bayesian synthesis inversion. They found that the differences in observational coverage of the ground-based and space-based data sets were complementary, resulting in smaller posterior uncertainty estimates when both data sets are assimilated than either data set alone. Similarly, in a set of regional Observing System Simulation Experiments (OSSEs), Fischer et al. (2017) showed reduced uncertainty in biosphere and fossil fuel emissions in California by combining space-based X_{CO₂} and surface-based flask and in situ measurements.

In this study, we further investigate combining ground-based and space-based measurements of atmospheric CO₂ to provide estimates of NEE globally, but we focus on northern extratropical regions where surface-based and aircraft-based measurements are most densely concentrated. We perform a series of 6-year flux inversions (2010–2015, inclusive) assimilating surface-based measurements from the in situ and flask measurement network, TCCON column-averaged dry-air CO₂ mole fractions (X_{CO₂}), GOSAT X_{CO₂} measurements, and all three data sets combined. For each set of measurements, we perform three flux inversions applying different prior NEE flux and error constraints. From the spread in posterior fluxes due to differences in prior constraints, we quantify the precision to which these data sets constrain posterior fluxes. Spatial structures in the posterior fluxes are examined through comparisons between posterior NEE-simulated X_{CO₂} and X_{CO₂} measurements from Orbiting Carbon Observatory 2 (OCO-2) and GOSAT. The accuracy of posterior NEE-simulated CO₂ is examined through comparisons with aircraft-based CO₂ measurements.

The paper is outlined as follows. Section 2 describes the measurements used in this study, and section 3 describes the flux inversion setup. The posterior CO₂ fields obtained by the flux inversions are compared

with OCO-2 and aircraft-based measurements in section 4.1. We then examine the 6-year mean seasonal cycle and annual net fluxes (section 4.2) and interannual variability (IAV) (section 4.3) obtained by the flux inversions. Finally, the implications of the results are discussed in section 5, and conclusions are given in section 6.

2. Data

2.1. Surface-Based In Situ and Flask Measurements

Surface-based measurements of boundary layer atmospheric CO₂ can be performed using an in situ gas analyzer or by taking a flask sample, which is then returned to a lab and analyzed. A number of different groups from around the world collect surface CO₂ observations. We assimilate measurements from version 4.1 of the GLOBALVIEW plus package (Cooperative global atmospheric data integration project, 2018; Masarie et al., 2014) and the Japan-Russia Siberian Tall Tower Inland Observation Network (JR-STATION) of nine tower sites in Siberia (Sasakawa et al., 2010, 2013).

The GLOBALVIEW v4.1 package incorporates data from many observing sites around the world and is specifically prepared for use in data assimilation studies. We include measurements from the Integrated Carbon Observation System (ICOS RI, 2019) in our analysis. We assimilate GLOBALVIEW v4.1 measurements from surface in situ and flask sites, tower sites, and ship-based measurements. Data are only assimilated if the measurements are assimilated by NOAA's CarbonTracker, version CT2017 (CT_assim = 0). Measurements are assimilated at the intake height above the model surface over land and at the intake height above sea level for ocean grid cells. For surface-based flask and in situ measurements, most of the measurement error applied for assimilation is due to representativeness errors (inability to model these measurements). We use the model-data mismatch (mdm) as the measurement errors. This is the error value placed on each measurement in the assimilation system and is meant to express the statistics of simulated minus-observed CO₂ residuals expected if CarbonTracker was using perfect surface fluxes.

JR-STATION is a network of nine towers (<http://www.cger.nies.go.jp/en/climate/pj1/tower/>). On these towers, high inlet measurements are obtained over 17–20 min of each hour, and the low inlet data are obtained from 37–40 min of each hour; these 3-min averages are then taken to be representative of the hourly means for each inlet. We filter the measurements by removing all measurements where the vertical gradient in CO₂ exceeds 0.5 ppm (to remove measurements when the boundary layer is not well mixed) and use the measured value at the highest intake for the measurement. For each site, the errors (in ppm) are prescribed to be constant throughout a given month; the errors range from 3 ppm in winter to 7 ppm in summer to account for both measurement and representativeness errors. These error estimates were chosen because they are comparable to the error estimates for tower sites in the GLOBALVIEW plus v4.1 package.

We remove outliers and poorly modeled measurements by filtering out measurements for which the difference between the prior NEE-simulated measurements and actual measurements exceeds three standard deviations of the measurement uncertainty (see section 3 for details on the forward model simulations). We also remove measurements for which the difference between prior simulated CO₂ and measurement exceeds 10 ppm, as these are assumed to be poorly simulated by the model. This filtering removes ~8% of the measurements. For each site, the data are only assimilated between 11 a.m. and 4 p.m. local time.

2.2. Aircraft-Based Measurements

Aircraft measurements are used for the evaluation of posterior atmospheric CO₂ fields. Aircraft data are obtained from the version 4.1 of the GLOBALVIEW plus data set. Comparisons between measured and modeled atmospheric CO₂ are performed over three distinct regions: East Asia, North America, and Alaska/Arctic (Figure S1 in the supporting information). Aircraft measurements over East Asia come exclusively from the Comprehensive Observation Network for Trace gases by Airliner (CONTRAIL) program (Machida et al., 2008, 2018). Aircraft data over Alaska/Arctic and North America originate from the NOAA Global Greenhouse Gas Reference Network's aircraft program (Sweeney et al., 2015) and HIAPER Pole-to-Pole Observations (HIPPO) (Wofsy, 2011). The number of hourly mean measurements per month between 3 and 8 km in altitude above sea level (asl) is shown in Figure S2.

Table 1
TCCON sites used in this study

Site Name	Lat	Lon	Start Date	Reference
Eureka	80.05°N	86.42°W	25 July 2010	Strong et al. (2017)
Orleans	47.97°N	2.11°E	29 August 2009	Warneke et al. (2017)
Park Falls	45.95°N	90.27°W	2 June 2004	Wennberg et al. (2017)
Rikubetsu	43.46°N	143.77°E	16 November 2013	Morino et al. (2017)
Lamont	36.60°N	97.49°W	6 July 2008	Wennberg et al. (2017)
Edwards	34.96°N	117.88°W	20 July 2013	Iraci et al. (2017)
Ascension Island	7.92°S	14.33°W	22 May 2012	Feist et al. (2017)
Darwin	12.46°S	130.93°E	28 August 2005	Griffith et al. (2017)
Reunion Island	20.90°S	55.49°E	16 September 2011	De Mazire et al. (2017)
Wollongong	34.41°S	150.88°E	26 June 2008	Griffith et al. (2017)

2.3. TCCON Measurements

TCCON is a network of ground-based Fourier transform spectrometers that record solar absorption spectra in the near infrared from which, among other gases, X_{CO_2} is estimated (Wunch et al., 2011). CO_2 abundances are retrieved using a nonlinear least squares approach from absorption lines in the near-infrared spectral region. The column-averaged dry-air mole fractions of CO_2 (X_{CO_2}) is calculated by taking the ratio of the column abundance of CO_2 to O_2 (scaled by the mean O_2 concentration), resulting in high-precision ($<0.25\%$ in CO_2) X_{CO_2} measurements. The TCCON strives to achieve the best site-to-site precision and accuracy possible. Systematic biases that are consistent throughout the network are accounted for by scaling the TCCON retrieval results to the WMO scale via aircraft and AirCore profiles (Wunch et al., 2010). Moreover, the TCCON sets guidelines to ensure that the instrumentation at each site is as similar as possible and that the retrieval software, including the spectroscopic line lists and line shapes, is identical for each site. However, site-specific differences (e.g., instrumental line shape) can cause residual site-to-site biases (Wunch et al., 2010) which might introduce biases in flux inversions.

For this study, TCCON data were obtained from the TCCON Data Archive, hosted by CaltechDATA (<https://tccodata.org>). We include data from TCCON sites that have mean biases of less than 0.5 ppm relative to both the OCO-2 target-mode X_{CO_2} and the posterior-simulated X_{CO_2} from the surface-only flux inversions. The sites included in this study, which provide data during the years 2010–2015, are given in Table 1. Sites that are excluded from this study are excluded due to several factors that cause apparent biases to be greater than 0.5 ppm. These factors may include: proximity to large CO_2 sources (e.g., cities), proximity to large topographic variability, and in a few cases, known TCCON instrument biases for which a solution either has been applied, or will be applied in an upcoming TCCON data version. Understanding the exact reason for the biases is beyond the scope of this study. Note that the threshold of 0.5 ppm is somewhat arbitrary. This value was set because most sites outside of this threshold are in heavily observed regions (e.g., Europe), which are expected to be well constrained by other data sets (Byrne et al., 2017), or in the Southern Hemisphere and not expected to have a large impact on the performance of the flux inversions in the northern midlatitudes.

In this study, the TCCON data are filtered to remove measurements with solar zenith angles greater than 70° . Measurements are then binned into hourly medians for each site. Only hours with five or more measurements are included. Measurements are only assimilated between 11 a.m. and 3 p.m. local time for the flux inversions, to minimize potential biases relating to errors in the prescribed diurnal cycle of NEE.

2.4. Space-Based Measurements

We assimilate X_{CO_2} measured by the Thermal And Near-infrared Sensor for carbon Observations Fourier Transform Spectrometer (TANSO-FTS) aboard GOSAT. GOSAT was launched in February 2009 in a Sun-synchronous orbit, with a repeat cycle of 3 days that produces 44 separate ground track repeats (Yoshida et al., 2013). The footprint of the GOSAT measurements has a diameter of about 10 km. Since August 2010, TANSO-FTS has been measuring with a 3-point cross-track pattern with 263-km cross-track separation, resulting in a swath of 526 km. Measurements have an along-track separation of 283 km (Crisp et al., 2012). We use version 7.3 of the NASA Atmospheric CO_2 Observations from Space (ACOS)

GOSAT measurements in this analysis. A detailed description of ACOS retrieval algorithm is available in O'Dell et al. (2012) and Crisp et al. (2012), with recent updates described in Eldering et al. (2017) and O'Dell et al. (2018). We only assimilate high gain (H-Gain) nadir measurements from the TANSO-FTS short-wave infrared (SWIR) band. We assimilate all H-Gain measurements that pass the quality flag requirement. These measurements are only over land.

Measurements from OCO-2 are used for comparisons with the posterior CO₂ fields. OCO-2, launched in July 2014, is a space-based spectrometer in a Sun-synchronous orbit that measures reflected solar radiation to infer X_{CO₂} with a footprint of about 3 km². It has a repeat cycle of 16 days, resulting in 233 separate ground track repeats. OCO-2 has a swath of 10 km and collects eight adjacent, spatially resolved samples every 0.333 s, resulting in roughly 24 soundings per second. We downloaded version 9 of the ACOS OCO-2 lite files from the CO₂ Virtual Science Data Environment (<https://co2.jpl.nasa.gov/>). Measurements are averaged into super-obs at 1° × 1° resolution grids following Liu et al. (2017), with the additional requirement that there must be a minimum of eight OCO-2 observations within each 1° × 1° grid box. We combine land nadir and land glint measurements for the analysis.

3. Flux Inversions

Flux inversions are performed with the Greenhouse Gas Framework – Flux (GHGF-Flux) inversion system. GHGF-Flux is a flux inversion system developed under the NASAs Carbon Monitoring System (CMS) project. The GHGF is capable of jointly assimilating multiplatform observations of CH₄, CO, CO₂, and OCS. The GHGF inherits the chemistry transport model from the GEOS-Chem and the adjoint model from the GEOS-Chem adjoint.

Chemical transport is driven by the Modern-Era Retrospective Analysis for Research and Applications, Version 2 (MERRA-2) meteorology produced with version 5.12.4 of the GEOS atmospheric data assimilation system (Gelaro et al., 2017). To perform tracer transport, these fields are regridded to 4° × 5° horizontal resolution and archived with a temporal resolution of 6 hr except for surface quantities and mixing depths, which have a temporal resolution of 3 hr. Tracer transport is performed at 30-min time steps with 47 vertical levels.

For all inversions, we optimize 14-day scaling factors for daily net NEE and ocean fluxes, except for the final temporal grouping of each year, which is padded with 1–2 days so that the groupings cover the same day-of-year increments for each year. We use an assimilation window of approximately 18 months (7 October to 1 April two years later) and keep posterior fluxes for one year (1 January to 31 December) then shift the inversion window forward one year. Using this method, we optimize NEE spanning 2010–2015. Initial conditions are generated by performing a two-year inversion of surface in situ and flask measurements spanning 1 January 2008 to 31 December 2009. The stratosphere is then adjusted to match the zonal mean structure of Diallo et al. (2017) for October 2009. This is performed by interpolating the climatology of Diallo et al. (2017) to the latitude-longitude grid of GEOS-Chem. Then, a scaling factor is applied each longitude grid cell for a given latitude-longitude location so that the zonal mean mole fraction matched the climatology. The magnitude of this correction was a few parts per million.

Prior NEE fluxes and errors differ between inversions and are generated from three different models: the simple biosphere model (SiB3), the Carnegie-Ames-Stanford Approach (CASA) model, and FLUXCOM. The motivation for using three different priors is to investigate the sensitivity of posterior fluxes to model structure differences in the prior fluxes and assumed prior uncertainties in each model (Philip et al., 2019). As shown in Huntzinger et al. (2017), the model structure differences in biogeochemical models are still a major source uncertainty. This method follows the Monte Carlo approach and is analogous to other flux inversion ensembles, such as those reported in Crowell et al. (2019). We sample three different prior NEE estimates, perform the flux inversion with each, and analyze the distribution of posterior fluxes. Due to the small ensemble, this method is less computationally expensive than methods that estimate the posterior errors (Chevallier et al., 2007). This method also has the advantage that it provides a more realistic error estimate in the case that the prescribed prior errors are not reflective of the true prior uncertainties (i.e., smaller errors are applied due to regularization requirements). As our uncertainty quantification is atypical, we provide a brief comparison of the magnitude of prior model spread and uncertainty. Figure S3 compares the relative magnitudes of the prior model spread (full-width) and 1 σ mean model uncertainty

($\sigma_{\text{mean}} = (\sigma_{\text{CASA}} + \sigma_{\text{SiB3}} + \sigma_{\text{FLUXCOM}})/3$). The root-mean-square (RMS) ratio of model spread to model uncertainty gives a metric of the relative magnitudes of model spread and uncertainty. We find that the ratio is temporally and spatially heterogeneous. On average, the model uncertainty exceeds the model spread for $4^\circ \times 5^\circ$ grid cells. (median ratio of 0.73 on 1 February, 0.97 on 1 May, and 0.89 on 1 August). However, model uncertainties are assumed to be spatially and temporally uncorrelated, whereas model structural differences are more coherent, such that the ratio of model spread to uncertainty increases with aggregation. For example, we obtain ratios of 3.3 for 1 February, 3.5 for 1 May, and 3.7 for 1 August for temperate North America. Thus, the magnitudes of model spread and model uncertainty are comparable, suggesting that the model spread employed here provides a reasonable estimate of uncertainty.

For all prior fluxes the annual total net flux has been adjusted to $4.6 \text{ PgC year}^{-1}$, to match the mean atmospheric CO_2 growth rate. This ensures that surface-based observations would not be prefiltered out (section 2.1) because the prior NEE has growth rate very different from observations. In addition, using prior that is consistent with observed global growth rate saves computation cost, since the inversion process will only need to adjust the NEE components that we do not have prior knowledge of. Details on the modeled NEE fluxes and prior errors are given in Appendix A. The diurnal cycle in NEE is prescribed using the modeled diurnal cycle from SiB3 for the SiB3 flux inversions and the diurnal cycle from CASA for the CASA and FLUXCOM inversions. Sensitivity tests found that the flux inversions were not sensitive to the prescribed diurnal NEE cycle. The ECCO-Darwin-V1 model (Brix et al., 2015; Dutkiewicz et al., 2009; Menemenlis et al., 2008) estimates are used as the prior ocean CO_2 exchange for all inversions, and prior errors were taken to be 100% of the flux. Fossil fuel, biofuel, and biomass burning CO_2 emissions are prescribed using the Open-source Data Inventory for Anthropogenic CO_2 , version 2018 (Oda & Maksyutov, 2011; Oda et al., 2018) with downscaling to hourly emissions based on Nassar et al. (2013), CASA-GFED4-FUEL, and Global Fire Emission Database, version 4 (GFED4) (Randerson et al., 2018) inventories, respectively.

Prior error covariance matrices are taken to be diagonal, such that there are no spatial or temporal covariances. The prior NEE errors are generated based on the NEE fluxes provided by the models. It is first taken to be 60% of the NEE flux. This is then increased by scaling up the errors at times and grid cells that have active vegetation but small net fluxes. For example, the uncertainty is scaled up during the spring (source to sink) and fall (sink to source) transition periods when the 14-day NEE flux is small but the summer 14-day NEE fluxes are much larger. We also inflate the uncertainty for grid cells in which the flux is small for a given model but is much larger for the other models. The final errors range from 100% to 500% of the NEE flux. Additional details are provided in Appendix A.

A series of flux inversions are performed that assimilate different data sets. This allows us to quantify the influence of different observational data sets on the posterior fluxes. We perform flux inversions that assimilate only ground-based in situ and flask measurements (referred to as surface-only), only TCCON measurements (TCCON-only), only GOSAT data (referred to as GOSAT-only), and all data sets simultaneously (referred to as GOSAT + surface + TCCON). For each data assimilation setup, we perform flux inversions with each of the three prior NEE fluxes and errors. Therefore, we perform a total of 12 flux inversions.

4. Results

4.1. Evaluation of Posterior NEE-Simulated CO_2

Large spatial structures in the posterior-simulated CO_2 fields are compared with GOSAT and OCO-2 X_{CO_2} , while the accuracy of the fluxes is evaluated against aircraft-based CO_2 measurements. Rather than describing the data-model differences for all 12 inversions, the posterior fluxes are grouped by the data set assimilated, and the mean posterior fluxes are evaluated. Tables giving the data-model mismatch between the individual flux inversions and aircraft measurements are provided as supplementary materials (Tables S1 and S2).

4.1.1. Comparison of Posterior CO_2 Against Space-Based X_{CO_2}

Space-based X_{CO_2} measurements have broad spatial coverage on the timescale of a month. This allows for comparisons between modeled and measured X_{CO_2} data over large spatial scales. Here, the data-model mismatch between the posterior CO_2 fields and space-based measurements from GOSAT and OCO-2 is examined. Figure 1 shows the zonal mean data-model mismatch as a function of latitude and time for the mean prior fluxes and mean posterior fluxes for the TCCON-only inversions, surface-only inversions,

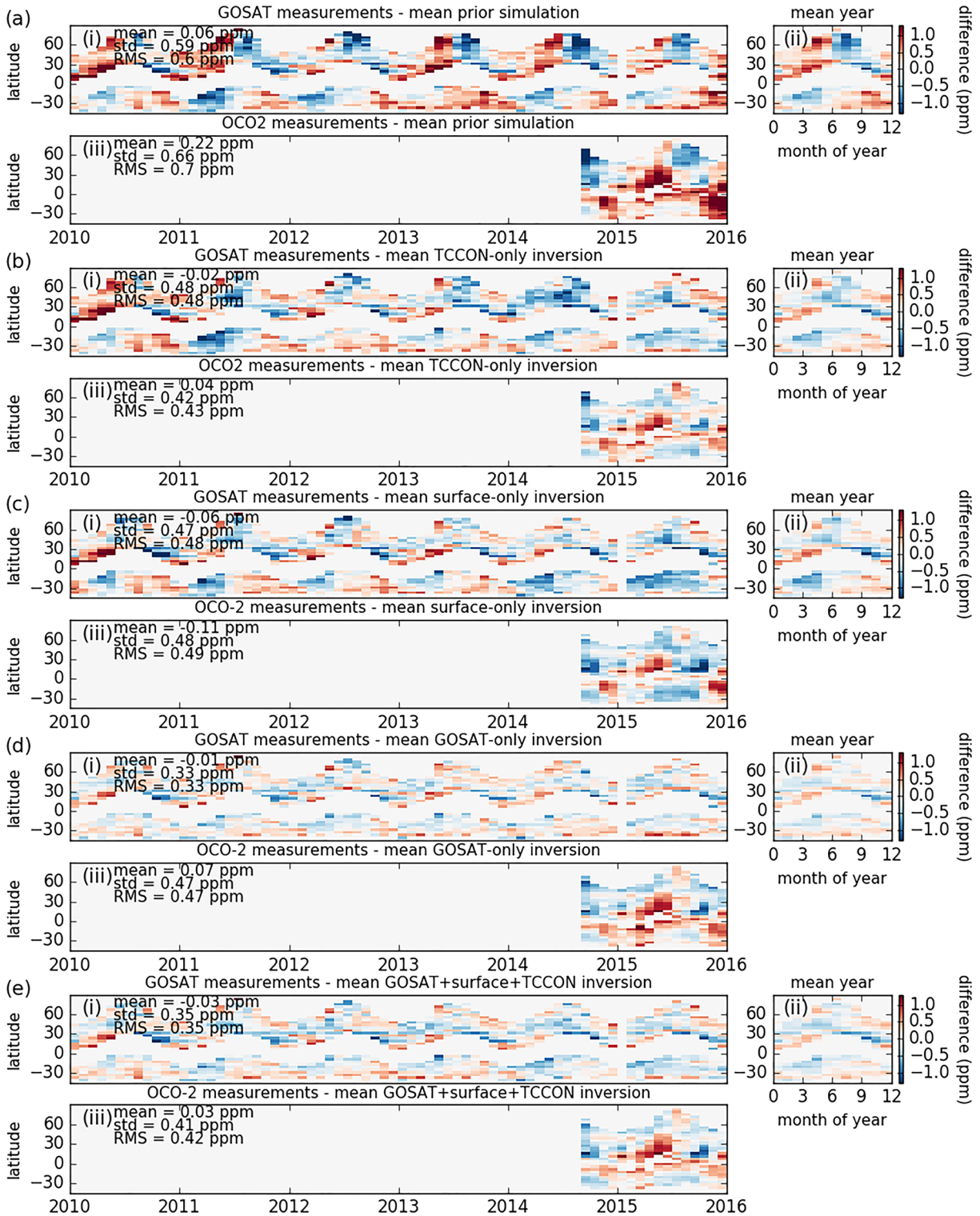


Figure 1. Zonal mean data-model mismatch for space-based X_{CO_2} measurements as a function of latitude and time for the (a) prior fluxes, (b) TCCON-only inversions, (c) surface-only inversions, (d) GOSAT-only inversions, and (e) GOSAT + surface + TCCON inversions. For each set of flux inversions, the three panels show (i) the zonal and monthly mean GOSAT X_{CO_2} data-model difference for 2010–2015. (ii) The mean GOSAT X_{CO_2} data-model difference for each month of the year. (iii) The zonal and monthly mean OCO-2 X_{CO_2} data-model difference for 2014–2015. Statistics are shown for the aggregated zonal mean data-model mismatches.

GOSAT-only inversions, and GOSAT + surface + TCCON inversions. Note that there are gaps due to GOSAT's observational coverage in the tropics and at high latitudes. The mean prior flux gives larger data-model standard deviations against GOSAT (0.59 ppm) and OCO-2 (0.67 ppm) than all of the flux inversions, implying that the flux inversions improve the variance of the data-model mismatch. The CO₂ fields simulated with the prior fluxes tend to be biased low relative to GOSAT and OCO-2 during the winter and spring and biased high during the summer and fall in the northern extratropics, suggesting that the prior fluxes underestimate the magnitude of the seasonal cycle. Comparing the posterior CO₂ fields against GOSAT, the surface-only and TCCON-only flux inversions give the largest mean data-model standard deviations, which is expected as these were the only inversions that do not assimilate GOSAT data.

Comparing to OCO-2, all of the flux inversions give similar differences. Mean differences range from −0.11 ppm to 0.07 ppm and standard deviations range over 0.41–0.48 ppm, suggesting that all of the flux inversions recover the global X_{CO₂} fields with similar accuracy and precision. However, north of 40°N, the GOSAT + surface + TCCON flux inversion shows better agreement with OCO-2 (RMS = 0.30 ppm) than the other flux inversions (RMS = 0.36–0.41 ppm). Differences between posterior-simulated X_{CO₂} and the OCO-2 measurements are largest in the northern subtropics, where the assimilated data sets have sparse observational coverage. Thus, it is unclear whether the differences in the subtropics are due to gaps in the observational coverage or possible biases between assimilated observations and OCO-2 retrievals.

The spread in simulated X_{CO₂} among the inversions gives a metric of the precision to which the flux inversion recovers atmospheric CO₂. Figure 2 shows the range of simulated GOSAT X_{CO₂} for the prior and posterior fluxes due to the different prior NEE fluxes and errors applied in the inversions. The largest range is obtained for the prior fluxes (1.37 ppm). The range for the TCCON-only and surface-only fluxes are reduced by 42% (0.79 ppm) and 64% (0.50 ppm) relative to the prior, respectively. Globally, the range for GOSAT-only and GOSAT + surface + TCCON inversions are reduced by 72% and 78%, respectively, relative to the prior. The decrease relative to the prior is largest in the northern extratropics. Differences in range between the GOSAT-only and GOSAT + surface + TCCON inversions are generally quite small. The most notable difference is that the GOSAT + surface + TCCON inversions have a smaller range in the northern extratropics during the fall. GOSAT measurements do not have high sensitivity to northern extratropical fluxes during this time of year (Byrne et al., 2017); thus, it appears that the surface-based measurements provide the additional information necessary to better constrain fall NEE in the northern extratropics. It is notable that the posterior-simulated GOSAT X_{CO₂} range is smallest for the GOSAT + surface + TCCON flux inversion, and that posterior data-model differences against GOSAT are similar for the GOSAT + surface + TCCON flux inversions and the GOSAT-only flux inversions. This implies consistent data quality among data sets and transport model reasonably captures vertical and boundary layer mixing.

For the surface-based in situ and flask flux inversions, and TCCON flux inversions, the posterior range increases in the tropics, where there is sparse observational coverage. For the GOSAT and GOSAT + surface + TCCON, the posterior range is generally reduced relative to the prior at all latitudes, although small increases in model spread occur in the northern tropics during the spring and southern tropics during the fall.

4.1.2. Evaluation of Posterior CO₂ Against Aircraft-Based Measurements

Aircraft-based measurements of atmospheric CO₂ provide a constraint on atmospheric CO₂ that is independent of the surface-based and space-based data sets assimilated. Therefore, aircraft-based CO₂ measurements offer a data set that modeled atmospheric CO₂ can be evaluated against. Evaluation of posterior CO₂ against aircraft-based measurements has previously been employed by a number of studies (Basu et al., 2014; Chevallier et al., 2019; Crowell et al., 2019; Frankenberg et al., 2016; Liu & Bowman, 2016; Peylin et al., 2007; Pickett-Heaps et al., 2011; Stephens et al., 2007). Here, we evaluate the atmospheric CO₂ fields simulated using the prior and posterior fluxes against aircraft measurements over three regions with intensive sampling: East Asia, North America, and Alaska/Arctic. We only use aircraft data between 3 and 8 km in altitude asl. Differences between measured and modeled CO₂ are due to both model transport errors and surface flux errors. We have found that the differences are strongly influenced by model transport errors for individual measurements but that the impact of representativeness errors on data-model mismatches is reduced with temporal aggregation; thus, we aggregate data-model mismatches to monthly means.

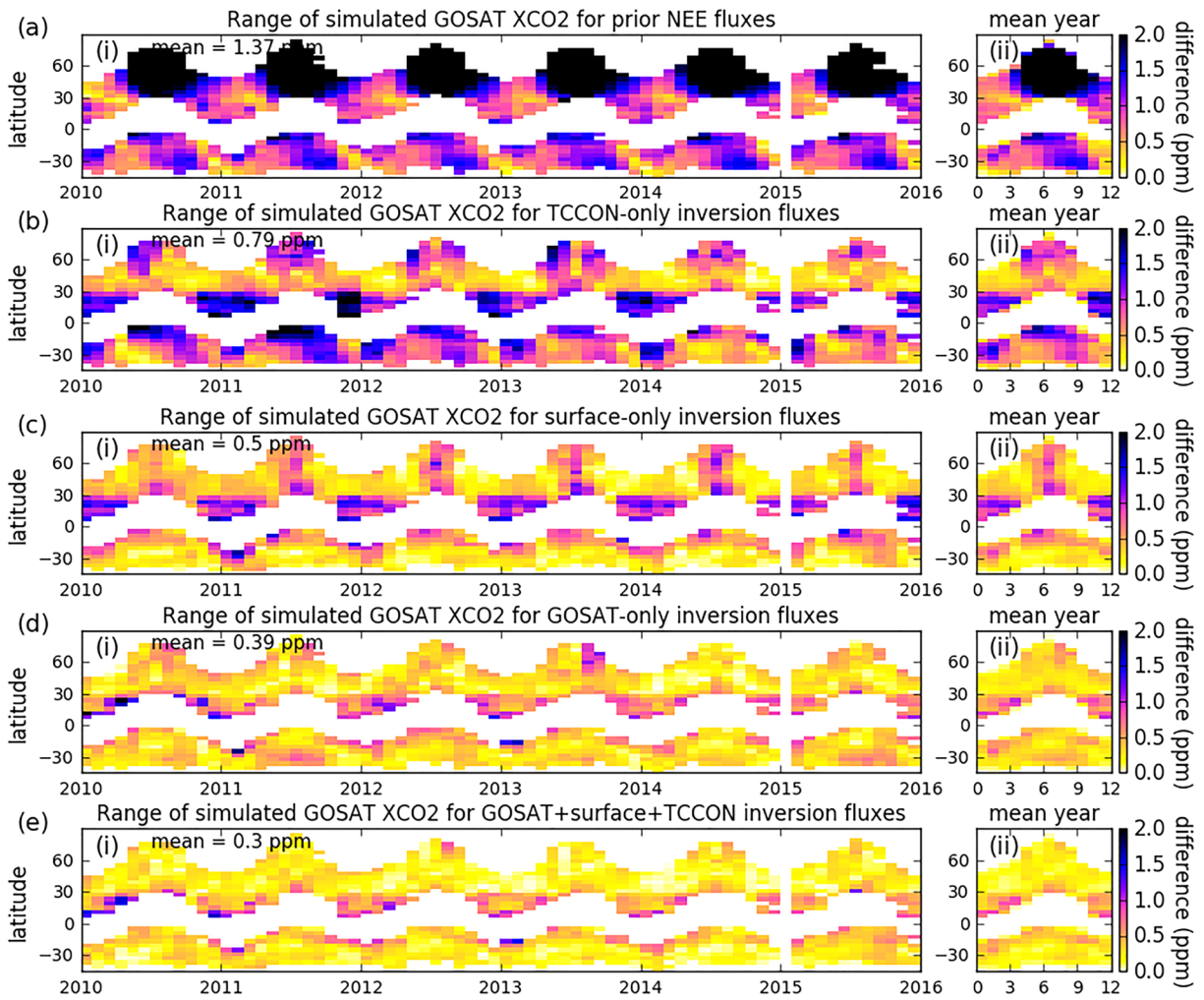
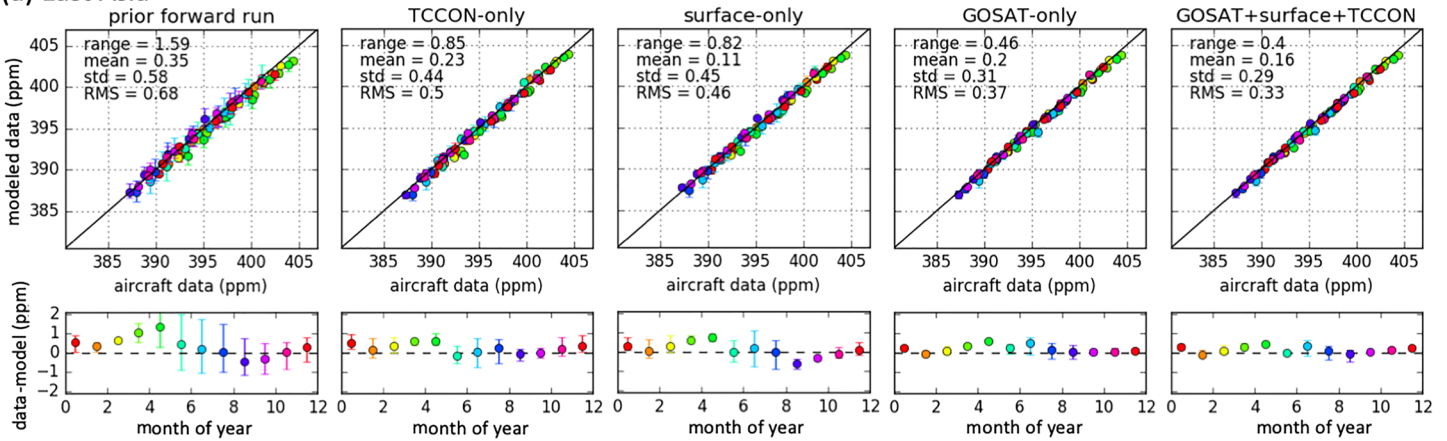


Figure 2. Spread in zonal and monthly mean simulated GOSAT X_{CO_2} for (a) prior NEE, (b) TCCON-only, (c) surface-only posterior NEE, (d) GOSAT-only posterior NEE, and (e) GOSAT + surface + TCCON posterior NEE as a function of latitude and time. For each set of flux inversions sets, the panels show (i) the zonal and monthly mean range for 2010 through 2015 and (ii) the mean range for each month of the year.

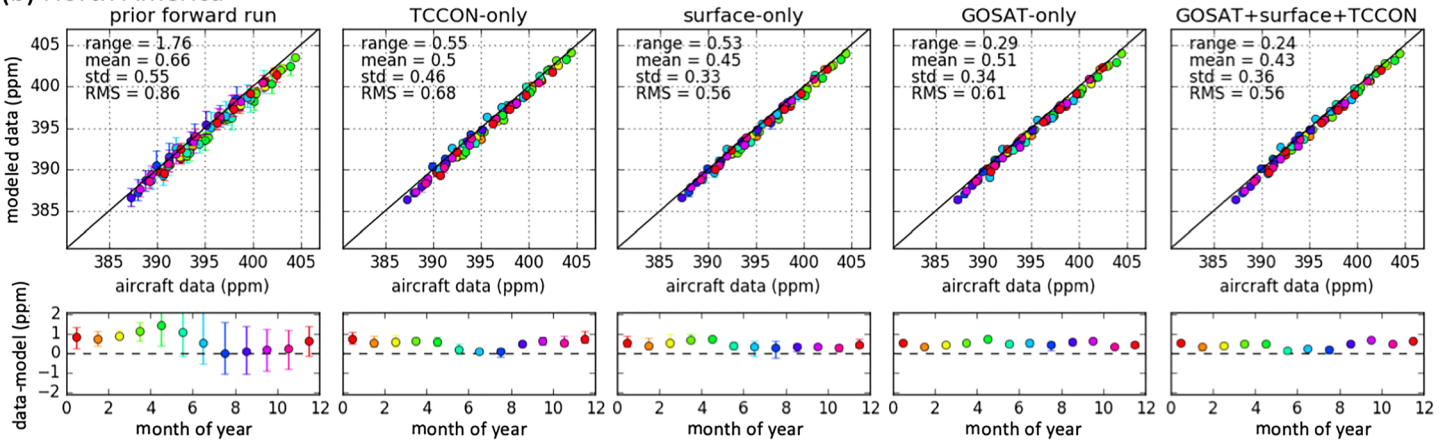
The GOSAT + surface + TCCON flux inversions generally show the best agreement with the aircraft-based CO_2 measurements. Figure 3 shows the monthly mean aircraft measurements and modeled CO_2 for the three regions examined here. The mean monthly range in data-model mismatch due to prior constraints is shown for each case, as are the mean, standard deviation, and RMS of data-model mismatch. This allows us to quantify the data-model mismatch relative to the spread due to prior constraints. For aircraft measurements over East Asia, North America, and Alaska/Arctic, we find that the prior range is large (1.59–2.55 ppm) relative to the RMS differences (0.68–1.14 ppm) indicating that aircraft observations are within the range of the prior simulated CO_2 . The posterior-simulated CO_2 measurements have much reduced ranges relative to the prior. For example, the GOSAT + surface + TCCON inversions give ranges of 0.24–0.40 ppm and RMS differences of 0.33–0.82 ppm across the regions, indicating that data-model differences are comparable to the precision of the posterior estimates.

Comparing the assimilated data sets, the GOSAT + surface + TCCON flux inversions give the smallest RMS difference against aircraft-based CO_2 in East Asia (0.33 ppm) and North America (0.56 ppm, equivalent to surface-only mismatch), and south of 30°N (0.61 ppm, Figure S4). The GOSAT-only flux inversions give the smallest RMS difference over the Alaska/Arctic region (0.77 ppm), although all of the flux inversions give larger RMS differences over this region relative to the midlatitude regions, suggesting that none of the flux inversions fully recover NEE at high latitudes. These aircraft measurements are also sensitive to fluxes over Siberia (Figure S5), which is poorly observed by all data sets. However, the larger RMS

(a) East Asia



(b) North America



(c) Alaska/Arctic

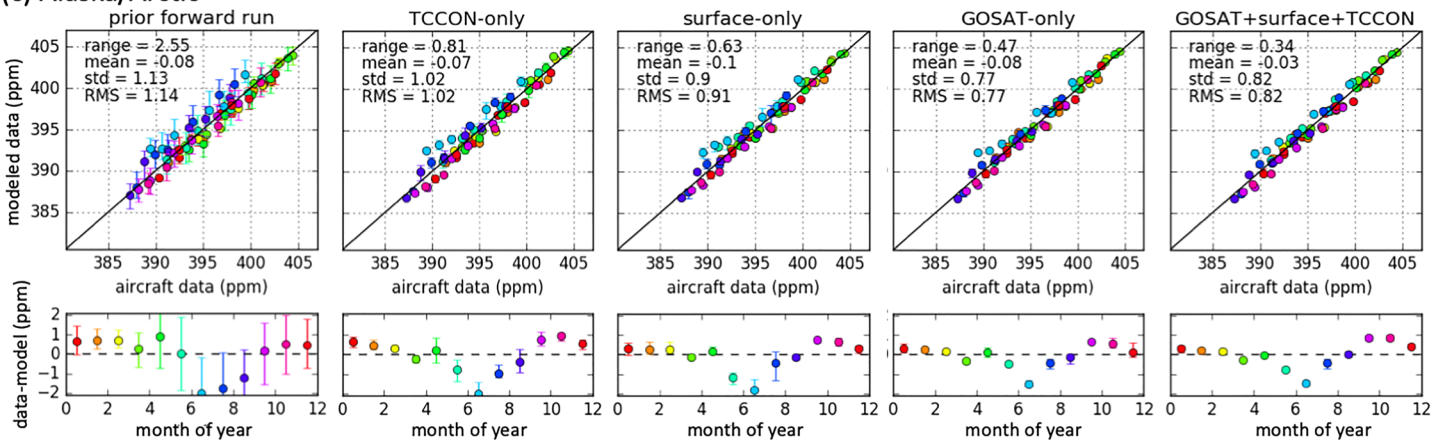


Figure 3. Comparison of monthly mean measured and simulated aircraft-based CO₂ for (a) East Asia, (b) North America, and (c) Alaska/Arctic. For each region, the mismatch for (left to right) prior, TCCON-only, surface-only, GOSAT-only, and GOSAT + surface + TCCON simulated CO₂ are shown. The top panel shows a scatter plot of the simulated aircraft-based CO₂ against the measured aircraft-based CO₂, and the error bars indicate the spread in posterior. Numbers in the top left corner show the mean posterior range, mean data-model mismatch, standard deviation of the data-model mismatch, and root-mean-square data-model mismatch. The lower panel shows the mean data-model mismatch for each month, with error bars showing the range of monthly mean mismatched between inversion setups. Colors correspond to the month of year.

differences over the Alaska/Arctic regions could also be due to transport model or representativeness errors. Differences in the data-model mismatch between flux inversions are evident as a function of month of year. The GOSAT + surface + TCCON flux inversion tends to best capture month-to-month variability, while both flux inversions assimilating GOSAT measurements tend to have less seasonality in the data-model mismatch than the TCCON-only and surface-only flux inversions. This is most evident for East Asia and suggests that the GOSAT-only flux inversions better capture the month-to-month variability in fluxes (consistent with the results of Polavarapu et al., 2018 & Byrne et al., 2019).

Despite these differences, the data-model biases against the aircraft-based measurements are generally similar between flux inversions. For example, all of the flux inversions give positive biases for East Asia (0.11–0.20 ppm, difference ≤ 0.09 ppm) and North America (0.45–0.51 ppm, difference ≤ 0.06 ppm) but negative biases for the Alaska/Arctic region (–0.07 to –0.01 ppm, difference ≤ 0.06 ppm). Therefore, the differences in posterior fluxes between inversions do not appear to be the largest driver of data-model biases. Transport model errors and representativeness errors may be primary drivers of regional data-model biases. We provide a lower bound estimate of transport model biases by regridding the fluxes and performing the evaluation against aircraft measurements at $2^\circ \times 2.5^\circ$ spatial resolution (Figure S6). Note that this is a lower bound estimate because there will be transport model errors common to both the $2^\circ \times 2.5^\circ$ and $4^\circ \times 5^\circ$ versions of GEOS-Chem (Yu et al., 2018). We find that model-data biases for the flux inversions change by 0.00–0.01 ppm for East Asia, 0.07–0.08 ppm for North America, and 0.09–0.10 ppm for Alaska/Arctic. These differences are similar to the magnitude of data-model differences between flux inversions, suggesting that transport model errors limit the ability of evaluating CO₂ flux estimates with aircraft-based measurements. This result is in contrast to Chevallier et al. (2019), who found that data-model mismatches were not strongly impacted by the version of Laboratoire de Météorologie Dynamique (LMDz) transport model employed.

4.2. Mean fluxes

4.2.1. Seasonal Cycle

In the northern extratropics, the seasonal cycle of NEE produces a large annual oscillation in atmospheric CO₂, giving seasonal variations of ~ 10 ppm in X_{CO_2} . This provides the largest signal of ecosystem carbon dynamics in atmospheric CO₂. In this section, we examine the seasonal cycle of NEE recovered by the flux inversions in the northern extratropics grouped by the assimilated data set. Figure 4 shows the seasonal cycle for the entire northern extratropics and five subcontinental regions (the spatial extent of the subcontinental regions are shown in Figure 5). We examine (1) the consistency in the seasonal cycle between the data sets and (2) the consistency of the posterior fluxes due to different prior assumptions.

The posterior seasonal cycles of the flux inversions show seasonal cycles with reduced spread relative to the prior for all assimilated data sets. The GOSAT + surface + TCCON NEE fluxes most closely match the GOSAT-only NEE fluxes during the summer, as GOSAT has dense observational coverage. During the winter, the GOSAT + surface + TCCON NEE fluxes most closely match the surface-only fluxes, particularly over temperate North America and Europe where the surface-based measurements are most densely concentrated.

The spread for each set of flux inversions shows the range in posterior fluxes due to differences in the prior fluxes and errors applied. This provides a metric of the precision to which the assimilated observations can constrain NEE. The spread is generally largest for the surface-only flux inversions outside of the winter. This is particularly notable over East Asia, where there is comparatively sparse observational coverage leading to a large spread among surface-only flux inversions. The spread is smallest for the GOSAT + surface + TCCON flux inversion, as expected. The small spread for the GOSAT + surface + TCCON flux inversions shows that the observational constraints provided by combining GOSAT, TCCON, and surface in situ and flask CO₂ measurements are sufficient to constrain the seasonal cycle of NEE on these subcontinental scales. These results suggest that the seasonal cycle is recovered by top-down flux inversions and suggests that analysis of the seasonal cycle of NEE, such as that presented by Byrne et al. (2018), could be extended to these regional scales. In the tropics and southern extratropics, the benefit of combining these data sets is somewhat reduced as the majority of information comes from GOSAT due to the sparsity of surface-based observations (Figures S7 and S8).

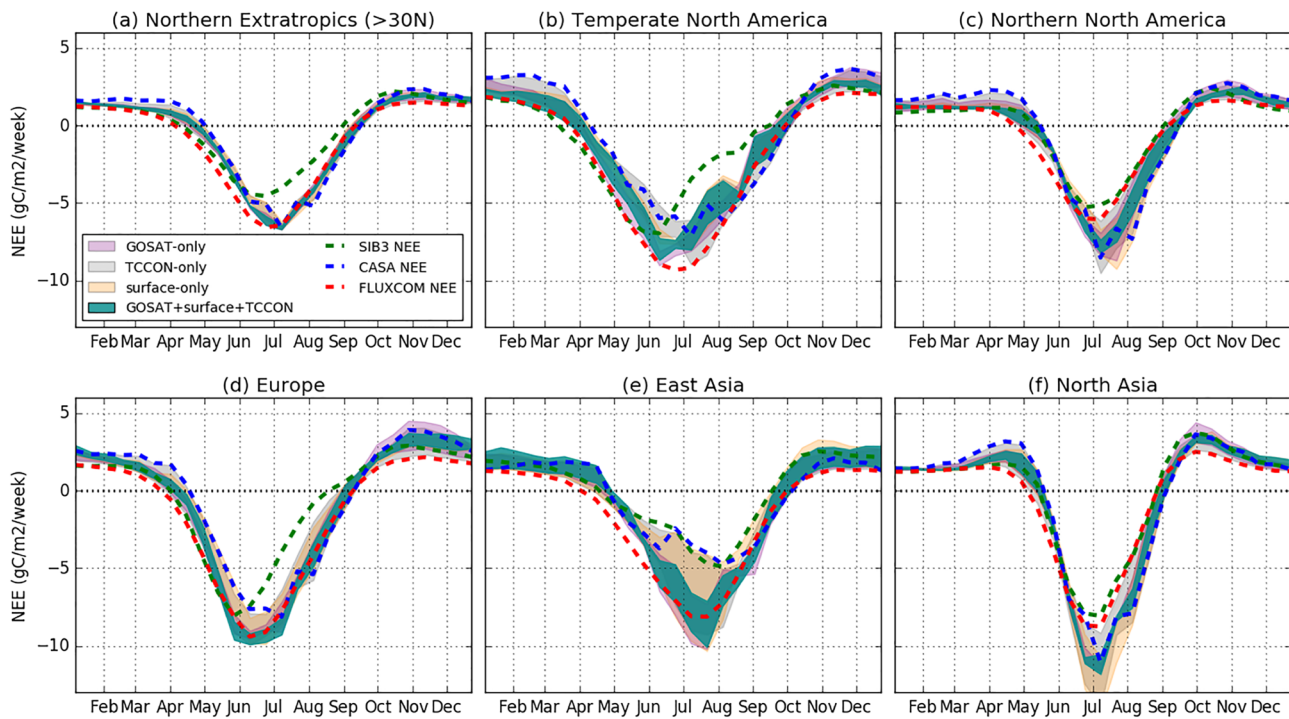


Figure 4. Prior and posterior NEE fluxes for (a) the entire northern extratropics (>30°N), (b) temperate North America, (c) northern North America, (d) Europe, (e) East Asia, and (f) North Asia at 14-day temporal resolution. The shaded curves show the range of posterior fluxes obtained by the GOSAT-only (purple), TCCON-only (gray), surface-only (yellow), and GOSAT + surface + TCCON (dark green) flux inversions. Dashed lines show the seasonal cycles for the three prior NEE fluxes used in inversions: SiB3 (green), CASA (blue), and FLUXCOM (red).

4.2.2. Annual Net Fluxes

Here, we examine the annual net fluxes obtained for the flux inversions over the northern extratropics. Figure 6 shows the 6-year mean annual net fluxes for each subcontinental region. Over the entire northern extratropics (>30°N), the flux inversions show high consistency relative to the spread in the prior. We obtain a mean annual net flux of $-2.80 \text{ PgC year}^{-1}$ (range of -3.43 to $-2.41 \text{ PgC year}^{-1}$) for the TCCON-only flux inversions, $-2.76 \text{ PgC year}^{-1}$ (range of -3.20 to $-2.49 \text{ PgC year}^{-1}$) for the surface-only flux inversions, $-2.89 \text{ PgC year}^{-1}$ (range of -3.31 to $-2.65 \text{ PgC year}^{-1}$) for the GOSAT-only flux inversions, and $-3.02 \text{ PgC year}^{-1}$

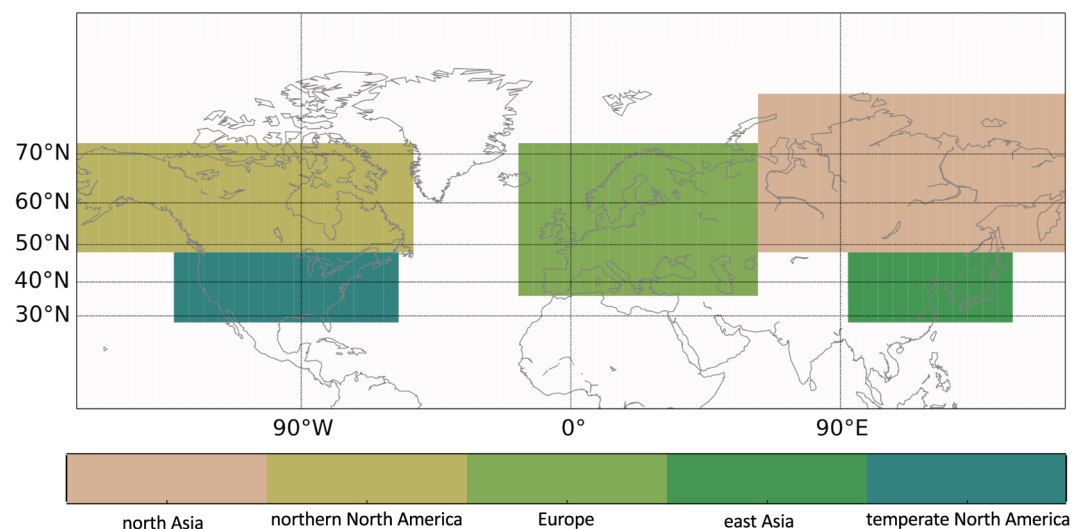


Figure 5. Five regions examined in this study. From left to right, the highlighted regions are referred to as northern North America, temperate North America, Europe, North Asia, and East Asia.

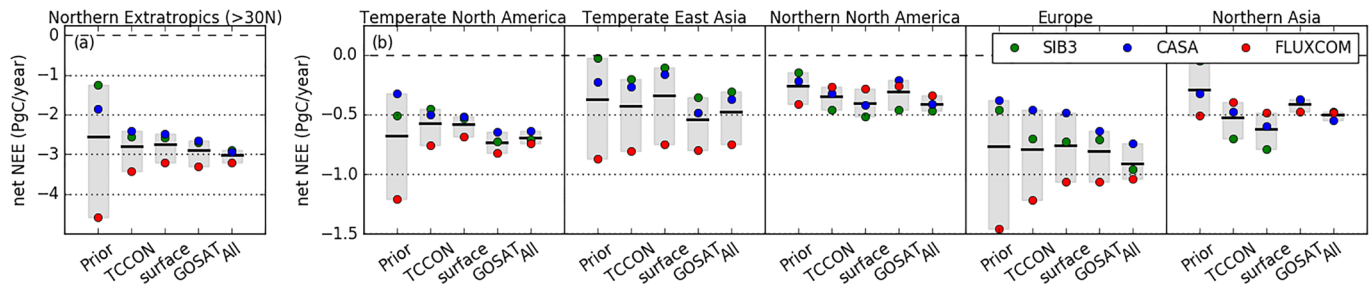


Figure 6. Six-year mean annual net NEE fluxes for (a) all of the northern extratropics and (b) the five regions examined in this study. Shaded gray regions show the range for the prior and posterior fluxes, while the solid black line shows the mean. Individual inversions are shown by the filled circles, with colors indicating prior NEE applied: green circles indicate SiB3, blue circles indicate CASA, and red circles indicate FLUXCOM. From left to right, the bars are for the prior (Prior), TCCON-only (TCCON), surface-only (surface), GOSAT-only (GOSAT), and GOSAT + surface + TCCON (All).

(range of -3.21 to -2.89 PgC year^{-1}) for the GOSAT + surface + TCCON flux inversions. It is notable that the prior assumptions applied to the flux inversions introduce substantial differences into the posterior fluxes. The range in the northern extratropical sink due to applying different prior NEE fluxes and errors is 0.32 – 1.03 PgC year^{-1} , depending on the assimilated data set.

On regional scales, there is generally overlap in the range of net annual fluxes between the TCCON-only, surface-only, GOSAT-only, and GOSAT + surface + TCCON flux inversions. This suggests that these observational data sets provide a consistent constraint on regional net annual NEE, within the considerable uncertainty introduced through prior assumptions. It is notable that the spread in net annual NEE due to prior constraints is as large as signals that have previously been reported between surface-based and space-based CO_2 measurements. For example, a larger European carbon sink of ~ 0.5 PgC year^{-1} has previously been obtained for GOSAT flux inversions relative to surface flask and in situ CO_2 flux inversions (Chevallier et al., 2014; Houweling et al., 2015; Reuter et al., 2014). However, the results found here show that the differences in sink between the surface-only and GOSAT-only are highly dependent on the prior constraints. For example, using FLUXCOM or SiB3 as priors result in similar European sinks. However, a larger sink is recovered in the GOSAT-only inversion if CASA is employed as the prior. Similar results are found in the tropics and Southern Hemisphere, although with increased spread (Figures S7 and S9).

4.3. Interannual Variability

IAV in NEE provides a measure of the response of ecosystems to climate variability. Here, we examine the IAV recovered by the flux inversions, where IAV is calculated to be the anomaly from the 6-year mean. Figure 7 shows the IAV in NEE for the entire northern extratropics and five extratropical regions at 14-day temporal resolution, after performing a 3-point (42-day) running mean to filter out high-frequency variability. The posterior NEE IAV is not sensitive to the prior NEE constraints applied in the flux inversion, such that similar posterior NEE IAV is recovered for each set of prior fluxes with a given assimilated data set. This is illustrated by the small range obtained for each set of colored curves. Similar results were found by Baker et al. (2006), who found that IAV was more robust than other measures. However, the posterior NEE IAV is sensitive to the assimilated data set, such that we find disagreement in NEE IAV for the TCCON-only, surface-only, and GOSAT-only flux inversions. Similar results are found in the tropical and Southern Hemisphere regions (Figure S10).

Differences in IAV between flux inversions can partially be explained by differences in the observational coverage of the data sets. As an example, let us consider the differences in IAV between the surface-only and GOSAT-only flux inversions in 2011 over temperate North America (Figure 8). This year was characterized by a “dipole” flux anomaly over North America, with a drought in the south (Texas-Mexico region) but with normal to above normal productivity in the northern USA – southern Canada (Liu et al., 2018; Byrne et al., 2019). Therefore, this provides a good case study to examine the ability of the inversion to capture structure in CO_2 fluxes. Figure 8a shows the monthly CO_2 anomalies observed by GOSAT and the surface in situ and flask network over the summer of 2011. GOSAT X_{CO_2} measurements are distributed uniformly across North America, while surface in situ and flask measurements are located south of Lake Superior. This observational coverage is reflected in the posterior fluxes. The GOSAT-only posterior NEE anomalies

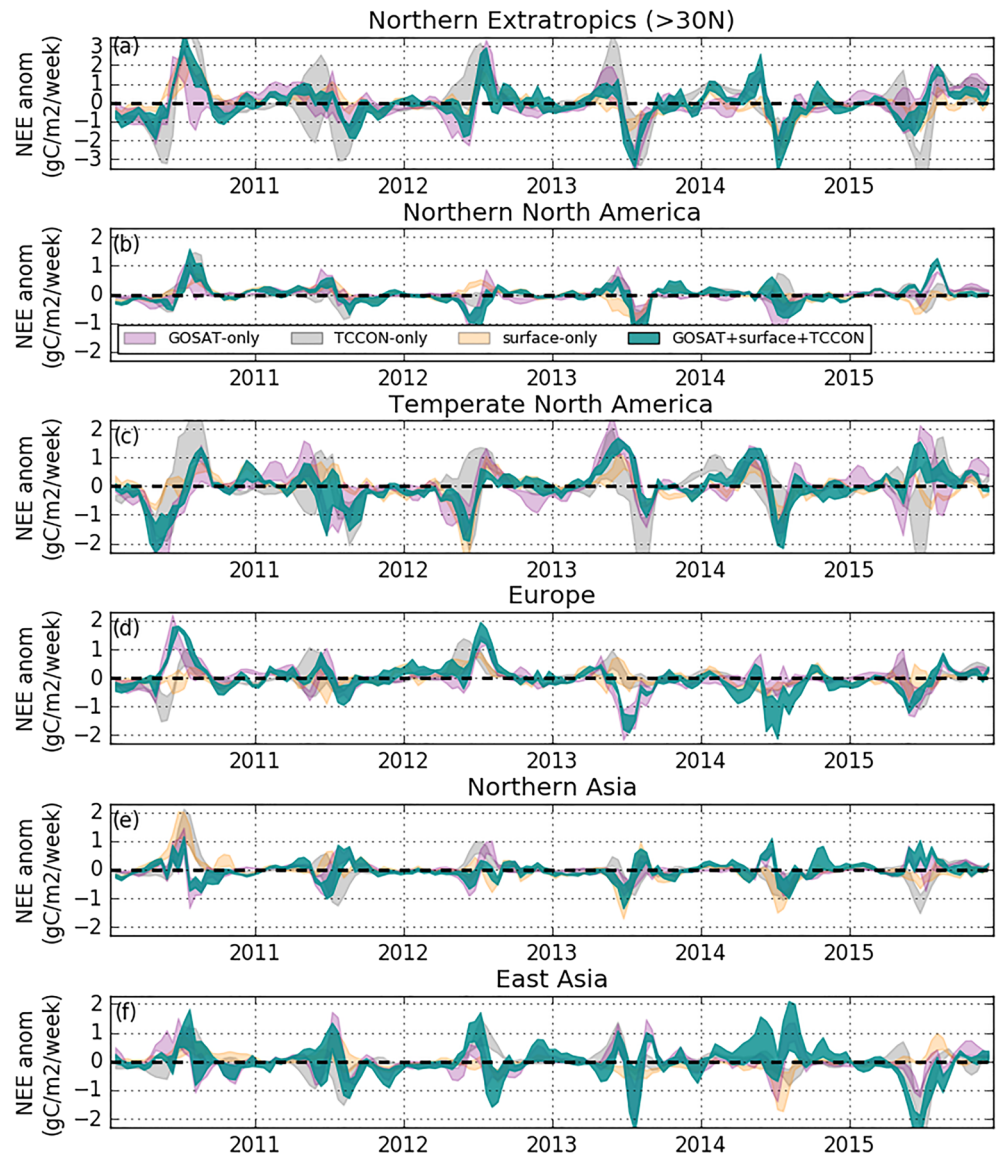


Figure 7. IAV in NEE for 2010–2015 at 14-day temporal resolution for (a) the entire northern extratropics ($>30^{\circ}\text{N}$), (b) northern North America, (c) temperate North America, (d) Europe, (e) North Asia, and (f) East Asia. The shaded curves show the range of posterior fluxes obtained by the GOSAT-only (purple), TCCON-only (gray), surface-only (yellow), and GOSAT + surface + TCCON (dark green) flux inversions. A 3-point (42-day) running mean is performed to remove high-frequency variability.

(Figure 8b) reflect the large scale structures in the X_{CO_2} anomalies but miss smaller scale structures, such as the positive anomalies over south central North America. The surface-only posterior anomalies (Figure 8c) capture smaller scale anomalies seen in CO_2 , such as the anomalous release of CO_2 in south central North America, but miss much of the large scale structures. Combining these two data sets in a single inversion, referred to as “GOSAT + surface,” captures both the large-scale structures from the GOSAT-only and small-scale structures from the surface-only flux inversion (Figure 8d). The posterior NEE anomalies from the GOSAT + surface flux inversion also correlate with anomalies in soil temperature (mean of MERRA-2 soil temperature over levels 1–3, Reichle et al., 2011, 2017) (Figure 8e) and soil moisture (ESA CCI Surface Soil Moisture Product, 1 nn Dorigo et al., 2017; Gruber et al., 2017; Liu et al., 2011; Liu et al., 2012; Wagner et al., 2012) (Figure 8f) over this time period, suggesting that combining these data sets produces more realistic NEE IAV. Similar results were found over Eurasia during the summer of 2010 (Figure S11).

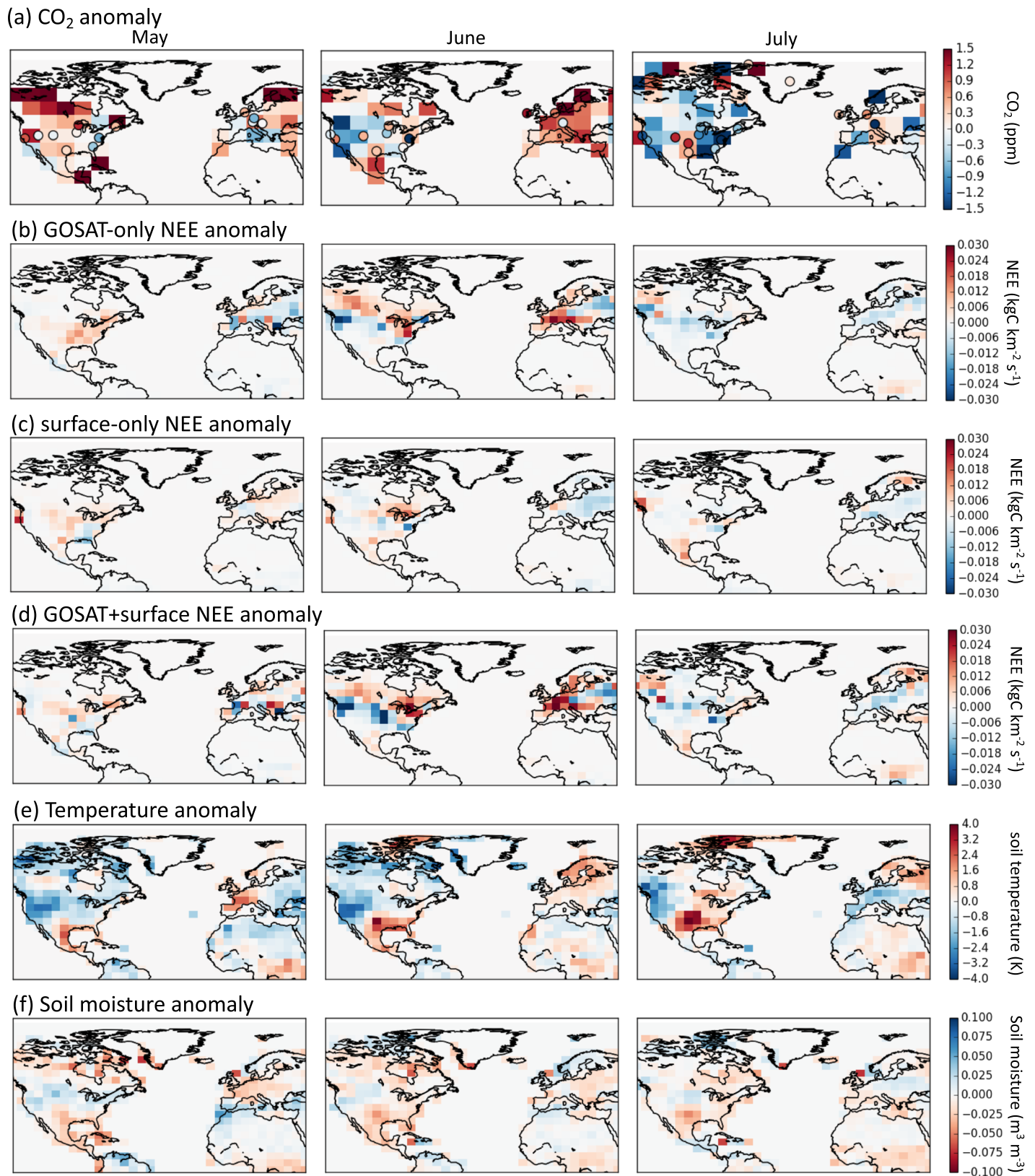


Figure 8. Monthly anomalies in (a) GOSAT X_{CO₂} (ppm, 4° × 5° grid cells) and surface site CO₂ (ppm divided by 4, circles), (b) GOSAT-only posterior NEE, (c) surface-only posterior NEE, (d) GOSAT + surface posterior NEE, (e) MERRA-2 soil temperature, and (f) ESA CCI soil moisture, for (left to right) May, June, and July of 2011.

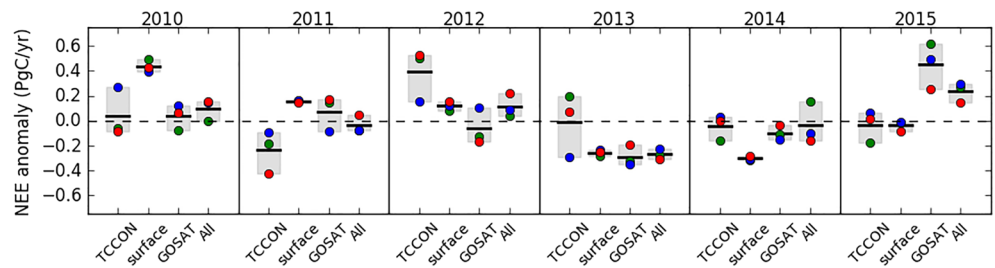


Figure 9. Annual net IAV in NEE over 2010–2015 for the TCCON-only, surface-only, GOSAT-only, and GOSAT + surface + TCCON flux inversions. Shaded gray regions show the range for the fluxes, while the solid black line shows the mean. Individual inversions are shown by the filled circles, with colors indicating prior NEE applied: green circles indicate SiB3, blue circles indicate CASA, and red circles indicate FLUXCOM.

On an annual basis, we find mixed agreement between flux inversions in year-to-year variations. Figure 9 shows IAV in annual net NEE anomalies for the entire northern extratropics. In general, IAV in annual net fluxes are consistent for a given set of assimilated data, suggesting that the results are not sensitive to the prior fluxes and errors used. Note that the prior NEE fluxes did not contain IAV, which has previously been shown to have a substantial impact on posterior NEE IAV (Byrne et al., 2019). However, posterior IAV is quite variable between different assimilated data sets. The cause of these differences between the flux inversions is likely partially due to differences in the observational coverage between data sets. It is possible that differences between data sets are also partially due to changes in the observational coverage over time, which has previously been shown to have an impact on inferred fluxes (Bruhwiler et al., 2011; Gurney et al., 2008; Rödenbeck et al., 2003).

5. Discussion

5.1. Consistency in Surface-Based and Space-Based Flux Constraints

The results generally show good agreement between the flux inversions assimilating different data sets. The agreement between the surface-only and GOSAT-only flux inversions may seem surprising in the context of a number of previous studies that have shown substantial differences between surface-based and space-based flux estimates (Basu et al., 2013; Chevallier et al., 2014; Houweling et al., 2015). However, more recent studies have shown improved agreement between surface-based and space-based flux inversions. Chevallier et al. (2019) found that flux inversions assimilating OCO-2 ACOS version 9 measurements gave similar net annual fluxes to those assimilating surface-based measurements and that both compared well against aircraft measurements. Interestingly, Chevallier et al. (2019) also found that GOSAT OCO Full Physics (OCFP) v7.1 XCO₂ retrievals did not compare as well against aircraft measurements. Comparisons between the ACOS 7.3 and OCFP v7.1 (downloaded from the Copernicus Climate Change Service: <https://climate.copernicus.eu/>) show substantial differences in zonal mean XCO₂ (Figure S12). Furthermore, GOSAT ACOS 7.3 retrievals are found to give better agreement with posterior-simulated CO₂ from the surface-only flux inversion (Figure S13). This suggests that the specific retrieval algorithm used can have a large impact on the posterior fluxes, such that the improved agreement between surface-based and space-based measurements found in recent studies may be primarily due to improvements in the ACOS XCO₂ retrieval algorithm. Miller and Michalak (2020) have also argued that recent improvements in the ACOS algorithm have substantially increased the reliability of OCO-2 XCO₂ measurements in flux inversions studies (for version 8 in particular). Substantial work has gone into refining the ACOS retrieval algorithm over the past decade (Crisp et al., 2012; Eldering et al., 2017; Kiel et al., 2019; Nelson & O'Dell, 2019; O'Dell et al., 2012; O'Dell et al., 2018). Thus, the improved agreement between surface-based and space-based CO₂ constraints is likely best explained by improvements in the ACOS retrieval algorithm.

A consistent 6-year mean northern extratropical sink is obtained by all observational data sets. This result is in contrast to several previous studies that found substantial differences in the annual net NEE flux of CO₂ in the northern extratropics between flux inversions assimilating surface-based and space-based measurements (Basu et al., 2013; Chevallier et al., 2014; Reuter et al., 2014; Saeki et al., 2013). The reason why

we obtain a more consistent annual net flux between data sets than some earlier studies is not immediately clear but could be due to advancements in the retrieval algorithm (e.g., ACOS 3.3 and earlier versions were used in Houweling et al., 2015) or due to the fact that we look at a multiyear mean, while earlier studies looked at shorter time periods (e.g., Houweling et al., 2015 only examined June 2009 to June 2010). In fact, we find that the surface-only inversion suggests weaker uptake in 2010 than average (by 0.40–0.49 PgC year⁻¹), while the GOSAT flux inversion suggests near average uptake (see section 4.3), suggesting that the difference in inferred fluxes between these two data sets may have been unusually large for 2010. However, it is important to note that differences in annual net fluxes do not imply biases in the measurements. There are aspects of the inversion setups that can lead to differences. For example, differences in the distribution of observations can lead to significant differences in annual net fluxes (Basu et al., 2018; Byrne et al., 2017; Collatz et al., 2014). Thus, one should not necessarily expect consistent annual net fluxes from observational data sets with spatial and temporal gaps in observational coverage.

It is notable that regional-scale annual net posterior NEE is generally found to be consistent between data sets, but IAV is not found to be consistent between data sets. This may be due to differences in the observational coverage between data sets, such that IAV in NEE is attributed to different regions.

5.2. Does Combining Data Sets Improve Flux Inversions?

Is it possible to conclude that the GOSAT + surface + TCCON flux inversions improve flux estimates relative to the flux inversions that assimilate a single data set? Of course, the answer to this question depends on how “improve” is defined. The GOSAT + surface + TCCON flux inversions generally show a small reduction in model-data differences against independent aircraft-based CO₂ and OCO-2 X_{CO₂} (north of 40°N). This suggests that combining these data sets in a flux inversion framework produces NEE fluxes that better recover the true atmospheric CO₂ fields than any data set alone. However, confounding factors in evaluating these fluxes remain a significant concern. Model transport errors appear to be a main driver of data-model differences for aircraft-based CO₂ measurements and obscure the source of data-model differences. Evaluating optimized fluxes against OCO-2 is also problematic because these retrievals are known to have their own biases.

The GOSAT + surface + TCCON flux inversions improve the precision of the posterior NEE fluxes relative to the flux inversions assimilating one data set. This is found to be the case at seasonal, annual, and interannual scales. The GOSAT + surface + TCCON flux inversions closely resemble the GOSAT-only NEE fluxes during the summer and surface-only fluxes during the winter for five northern extratropical regions. This is expected given the spatiotemporal distribution of GOSAT and surface-based CO₂ measurements and suggests that the GOSAT + surface + TCCON posterior NEE fluxes are better constrained by the observations than the GOSAT-only or surface-only flux inversions. Therefore, the GOSAT + surface + TCCON flux inversions are less likely to be impacted by biases in the observational coverage, such that, from an observational coverage perspective, we can conclude that the GOSAT + surface + TCCON flux inversions are better constrained than the GOSAT-only or surface-only flux inversions.

An important concern in combining CO₂ data sets within a single flux inversion system is that there could be relative biases in the atmospheric CO₂ constraints provided by the different data sets. Any inconsistency in flux constraints between data sets has the potential of introducing artifacts into the posterior fluxes. Biases in the observations could be present due to errors in the X_{CO₂} retrieval algorithm, representativeness errors (Agusti-Panareda et al., 2019) or model transport errors. Several previous studies have suggested that unrealistically large uptake over Europe (~1.5 PgC year⁻¹) is recovered in posterior fluxes due to biases in the GOSAT retrieval algorithm (Basu et al., 2013; Chevallier et al., 2014), although the ACOS retrieval algorithm has undergone significant development since these studies (Eldering et al., 2017; O'Dell et al., 2018) resulting in reduced biases (Miller & Michalak, 2020). Similarly, a number of studies have pointed out systematic transport errors in GEOS-Chem (Schuh et al., 2019; Yu et al., 2018), as well as biases in reanalysis winds (e.g., vertical mixing, Parazoo et al., 2012). We do not find clear evidence for biases between the surface-based and GOSAT constraints, although these biases may be challenging to identify. We also note that we perform filtering of TCCON and surface flask and in situ measurements to remove outliers, which makes the data sets more consistent than they would be without filtering. However, we do see the impact

of model transport errors in comparisons between the posterior-simulated CO₂ and aircraft measurements. Ideally, this analysis should be performed with two different transport models so that transport related errors could be more easily identified.

6. Conclusions

This study presented a series of flux inversions assimilating surface-based flask and in situ CO₂ measurements, TCCON X_{CO₂}, GOSAT X_{CO₂}, or all data sets combined. All of the flux inversions showed improved agreement with independent aircraft-based CO₂ measurements relative to prior flux estimates. The GOSAT + surface + TCCON flux inversion gave the smallest RMS differences against aircraft-based CO₂ measurements over East Asia and North America, and OCO-2 X_{CO₂} measurements (north of 40°N), suggesting that combining the data sets improves flux estimates. However, the data-model mismatches were strongly impacted by transport model spatial resolution, which makes robust evaluations of posterior surface fluxes challenging.

We found that all observing systems generally give reduced spread in posterior NEE fluxes relative to the prior fluxes. This suggests that these data sets provide consistent information on NEE. The GOSAT + surface + TCCON posterior NEE most closely resembles the GOSAT-only posterior NEE during the summer and surface-only posterior NEE during the winter, consistent with the temporal variations in the observational constraints. This suggests that the GOSAT + surface + TCCON flux inversions benefit from the improved spatiotemporal distribution of measurements, providing posterior fluxes that are better informed by measurements throughout the year.

The results of this study suggest that surface-based and space-based atmospheric CO₂ constraints provide consistent constraints on NEE fluxes and can be combined in a flux inversion framework. This result stands in contrast to earlier attempts to combine these data sets (Houweling et al., 2015) and suggests that the improved consistency between the data sets has been made possible by the considerable effort spent refining the ACOS retrieval algorithm (Chevallier et al., 2019; Eldering et al., 2017; Kiel et al., 2019; Miller & Michalak, 2020; O'Dell et al., 2018).

Appendix A: Prior NEE Fluxes and Errors

A1. Simple Biosphere Model

SiB3 was originally designed as a lower boundary for General Circulation Models with explicit treatment of biophysical processes. The ability to ingest satellite phenology was later introduced (Sellers et al., 1996; Sellers et al., 1996), and further refinements included a prognostic canopy air space (Vidale & Stöckli, 2005), more realistic soil and snow (Baker et al., 2003) and modifications to calculations of root water uptake and soil water stress (Baker et al., 2008). The current version is called SiB3. Simulations used in this analysis use phenology (leaf area index [LAI]; fraction of photosynthetically active radiation [fPAR]) from the Moderate Resolution Imaging Spectroradiometer (MODIS). MERRA reanalysis is used as model inputs, with precipitation scaled to Global Precipitation Climatology Project (GPCP; Adler et al., 2003) following Baker et al. (2010).

These fluxes are adjusted to obtain a global net drawdown equal to 4.6 PgC year⁻¹. To do this, the annual net flux at each grid cell and global total annual net drawdown are calculated. The annual net flux at each grid cell is then scaled so that the annual net flux is 4.6 PgC year⁻¹. The difference between the original and scaled annual net flux at each grid cell is then calculated. From this difference, an adjustment at each grid cell for each 14-day period is performed so that the annual net flux then equals the scaled annual net flux at each grid cell.

The prior NEE errors are generated based on the NEE fluxes provided by the models. It is first taken to be 60% of the NEE flux. This is then increased by scaling up the errors if the mean flux for a given grid cell is large but the flux is small at a given time. For example, the uncertainty is scaled up during the fall. We also inflate the uncertainty where the flux is small for SiB3 but large for CASA and FLUXCOM. The final errors range from 100% to 500% of the NEE flux. This results in a global annual error of 0.42 PgC year⁻¹.

A2. CASA

The version of the model used here, CASA-GFED3, was modified from Potter et al. (1993) as described in Randerson et al. (1996) and van der Werf et al. (2006). It is driven by MERRA reanalysis and satellite-observed NDVI to track plant phenology. We use the same fluxes as are used for the CarbonTracker 2016 (<https://www.esrl.noaa.gov/gmd/ccgg/carbontracker/>) prior. CASA outputs monthly fluxes of Net Primary Productivity (NPP) and heterotrophic respiration (R_H). From these fluxes, GPP and ecosystem respiration (R_e) are estimated to be $GPP=2NPP$ and $R_e=R_H-NPP$. Temporal downscaling and smoothing were performed from monthly CASA fluxes to 90-min fluxes using temperature and shortwave radiation from the ECMWF ERA-interim reanalysis (note this method differs from Olsen and Randerson (2004)). GFED_CMS is used for global fire emissions (<http://nacp-files.nacarbon.org/nacp-kawa-01/>). We use average model fluxes by averaging the fluxes for 2007–2012.

These fluxes are adjusted to obtain a global net drawdown equal to $4.6 \text{ PgC year}^{-1}$. To do this, the annual net flux at each grid cell and global total annual net drawdown are calculated. The annual net flux at each grid cell is then scaled so that the annual net flux is $4.6 \text{ PgC year}^{-1}$. The difference between the original and scaled annual net flux at each grid cell is then calculated. From this difference, an adjustment at each grid cell for each 14-day period is performed so that the annual net flux then equals the scaled annual net flux at each grid cell.

The prior NEE errors are generated based on the NEE fluxes provided by the models. It is first taken to be 60% of the NEE flux. This is then increased by scaling up the errors if the mean flux for a given grid cell is large, but the flux is small at a given time. For example, the uncertainty is scaled up during the fall. We also inflate the uncertainty where the flux is small for CASA but large for SiB3 and FLUXCOM. The final errors range from 100% to 500% of the NEE flux. This results in a global annual error of $0.31 \text{ PgC year}^{-1}$.

A3. FLUXCOM

FLUXCOM products are generated using upscaling approaches based on machine learning methods that integrate FLUXNET site level observations, satellite remote sensing, and meteorological data (Jung et al., 2017; Tramontana et al., 2016). Jung et al. (2017) generate R_e products using several machine learning methods. For this study, we downloaded the products generated using random forests (RFs), multivariate regression splines (MARS), and artificial neural networks (ANNs) at daily resolution from the Data Portal of the Max Planck Institute for Biochemistry (<https://www.bgc-jena.mpg.de>). The mean seasonal cycle over 2008–2012 is calculated for each product.

These fluxes are adjusted to obtain a global net drawdown equal to $4.6 \text{ PgC year}^{-1}$. For FLUXCOM, we only adjust fluxes south of 35°N because the northern extratropical NEE fluxes have been heavily informed by FLUXNET sites. For grid cells south of 35°N , the annual net flux at each grid cell and global total annual net drawdown are calculated. The annual net flux at each grid cell is then scaled so that the annual net flux is $4.6 \text{ PgC year}^{-1}$. The difference between the original and scaled annual net flux at each grid cell is then calculated. From this difference, an adjustment at each grid cell for each 14-day period is performed so that the annual net flux then equals the scaled annual net flux at each grid cell.

The prior NEE errors are generated based on the NEE fluxes provided by the models. It is first taken to be 60% of the NEE flux. This is then increased by scaling up the errors if the mean flux for a given grid cell is large but the flux is small at a given time. For example, the uncertainty is scaled up during the fall. We also inflate the uncertainty where the flux is small for FLUXCOM but large for SiB3 and CASA. The final errors range from 100% to 500% of the NEE flux. This results in a global annual error of $0.30 \text{ PgC year}^{-1}$.

Data Availability Statement

TCCON data were obtained from the TCCON Data Archive, hosted by CaltechDATA (<http://tccodata.org>). FLUXCOM products were obtained from the Data Portal of the Max Planck Institute for Biochemistry [<https://www.bgc-jena.mpg.de>]. MERRA-2 products were downloaded from MDISC (<https://gmao.gsfc.nasa.gov/reanalysis/MERRA-2/>), managed by the NASA Goddard Earth Sciences (GES) Data and Information Services Center (DISC). GOSAT OCFP v7.1 X_{CO_2} retrievals were downloaded from the Copernicus Climate Change Service website (<https://cds.climate.copernicus.eu>). Version 4.1 of the

GLOBALVIEW plus package was downloaded from <http://www.esrl.noaa.gov/gmd/ccgg/obspack/>. ESA CCI soil moisture data was downloaded from <https://www.esa-soilmoisture-cci.org/>. Odiac emissions data set was provided by T. Oda of Colorado State University, Fort Collins CO, USA/Global Monitoring Division, NOAA Earth System Research Laboratory, Boulder CO, USA. GOSAT and OCO-2 ACOS retrievals were downloaded from the CO₂ virtual science data environment: <https://co2.jpl.nasa.gov/>. Prior and posterior NEE and Ocean fluxes presented in this study will be available for download from <https://data.nasa.gov> and <https://cmsflux.jpl.nasa.gov/>. The JR-STATION data set is available from the Global Environmental Database, hosted by Center for Global Environmental Research (CGER), National Institute for Environmental Studies (NIES) (<http://db.cger.nies.go.jp/portal/geds/atmosphericAndOceanicMonitoring>).

Acknowledgments

BB was supported by an appointment to the NASA Postdoctoral Program at the Jet Propulsion Laboratory, administered by Universities Space Research Association under contract with NASA. JL was supported by the NASA OCO2/3 science team program NNH17ZDA001N-OCO2. KWB was supported by the NASA Carbon Monitoring System (CMS) project (NNH16ZDA001N-CMS). The research carried out at the Jet Propulsion Laboratory, California Institute of Technology, was under a contract with the National Aeronautics and Space Administration. Resources supporting this work were provided by the NASA High-End Computing (HEC) Program through the NASA Advanced Supercomputing (NAS) Division at Ames Research Center. Odiac project is supported by Greenhouse Gas Observing SATellite (GOSAT) project, National Institute for Environmental Studies (NIES), Japan. We thank S. Basu for providing downscaled ODIAC emissions. We thank T. Machida, H. Matsueda, Y. Sawa, and Y. Niwa for providing CONTRAIL measurements. The TCCON site at Reunion Island is operated by the Royal Belgian Institute for Space Aeronomy with financial support in 2014, 2015, 2016, 2017, 2018, and 2019 under the EU project ICOS-Inwire and the ministerial decree for ICOS (FR/35/IC2) and local activities supported by LACy/UMR8105 Universit de La Reunion. The TCCON project for Rikubetsu site is supported in part by the GOSAT series project. The Ascension Island TCCON station has been supported by the European Space Agency (ESA) under grant 4000120088/17/1-EF and by the German Bundesministerium für Wirtschaft und Energie (BMWi) under grants 50EE1711C and 50EE1711E. We thank the ESA Ariane Tracking Station at North East Bay, Ascension Island, for hosting and local support.

References

Adler, R. F., Huffman, G. J., Chang, A., Ferraro, R., Xie, P. P., Janowiak, J., et al. (2003). The version-2 Global Precipitation Climatology Project (GPCP) monthly precipitation analysis (1979–present). *Journal of Hydrometeorology*, 4(6), 1147–1167. [https://doi.org/10.1175/1525-7541\(2003\)004<1147:TVGPCP>2.0.CO;2](https://doi.org/10.1175/1525-7541(2003)004<1147:TVGPCP>2.0.CO;2)

Agusti-Panareda, A., Diamantakis, M., Massart, S., Chevallier, F., Muñoz Sabater, J., Barré, J., & Wunch, D. (2019). Modelling CO₂ weather—Why horizontal resolution matters. *Atmospheric Chemistry and Physics*, 19(11), 7347–7376. <https://doi.org/10.5194/acp-19-7347-2019>

Bacastow, R. (1976). Modulation of atmospheric carbon dioxide by the Southern Oscillation. *Nature*, 261(5556), 116–118. <https://doi.org/10.1038/261116a0>

Baker, I., Denning, A. S., Hanan, N., Prihodko, L., Uliasz, M., Vidale, P. L., & Bakwin, P. (2003). Simulated and observed fluxes of sensible and latent heat and CO₂ at the WLEF-TV tower using SIB2.5. *Global Change Biology*, 9(9), 1262–1277. <https://doi.org/10.1046/j.1365-2486.2003.00671.x>

Baker, I. T., Denning, A. S., & Stöckli, R. (2010). North American gross primary productivity: Regional characterization and interannual variability. *Tellus B*, 62(5), 533–549. <https://doi.org/10.1111/j.1600-0889.2010.00492.x>

Baker, D., Law, R. M., Gurney, K. R., Rayner, P., Peylin, P., Denning, A., et al. (2006). TransCom 3 inversion intercomparison: Impact of transport model errors on the interannual variability of regional CO₂ fluxes, 1988–2003. *Global Biogeochemical Cycles*, 20, GB1002. <https://doi.org/10.1029/2004GB002439>

Baker, I., Prihodko, L., Denning, A., Goulden, M., Miller, S., & Da Rocha, H. (2008). Seasonal drought stress in the Amazon: Reconciling models and observations. *Journal of Geophysical Research*, 113, G00B01. <https://doi.org/10.1029/2007JG000644>

Basu, S., Baker, D. F., Chevallier, F., Patra, P. K., Liu, J., & Miller, J. B. (2018). The impact of transport model differences on CO₂ surface flux estimates from OCO-2 retrievals of column average CO₂. *Atmospheric Chemistry and Physics*, 18, 10. <https://doi.org/10.5194/acp-18-7189-2018>

Basu, S., Guerlet, S., Butz, A., Houweling, S., Hasekamp, O., Aben, I., et al. (2013). Global CO₂ fluxes estimated from GOSAT retrievals of total column CO₂. *Atmospheric Chemistry and Physics*, 13(17), 8695–8717. <https://doi.org/10.5194/acp-13-8695-2013>

Basu, S., Krol, M., Butz, A., Clerbaux, C., Sawa, Y., Machida, T., & Aben, I. (2014). The seasonal variation of the CO₂ flux over Tropical Asia estimated from GOSAT, CONTRAIL, and IASI. *Geophysical Research Letters*, 41, 1809–1815. <https://doi.org/10.1002/2013GL059105>

Bolin, B., & Keeling, C. (1963). Large-scale atmospheric mixing as deduced from the seasonal and meridional variations of carbon dioxide. *Journal of Geophysical Research*, 68(13), 3899–3920. <https://doi.org/10.1029/JZ068i013p03899>

Bowman, K., Liu, J., Bloom, A., Parazoo, N., Lee, M., Jiang, Z., et al. (2017). Global and Brazilian carbon response to El Niño Modoki 2011–2010. *Earth and Space Science*, 4(10), 631. <https://doi.org/10.1002/2016EA000204>

Brix, H., Menemenlis, D., Hill, C., Dutkiewicz, S., Jahn, O., Wang, D., & Zhang, H. (2015). Using Greens Functions to initialize and adjust a global, eddying ocean biogeochemistry general circulation model. *Ocean Modelling*, 95, 1–14. <https://doi.org/10.1016/j.ocemod.2015.07.008>

Bruhwyler, L., Michalak, A., & Tans, P. (2011). Spatial and temporal resolution of carbon flux estimates for 1983–2002. *Biogeosciences*, 8(5), 1309–1331. <https://doi.org/10.5194/bg-8-1309-2011>

Byrne, B., Jones, D. B. A., Strong, K., Polavarapu, S. M., Harper, A. B., Baker, D. F., & Maksyutov, S. (2019). On what scales can GOSAT flux inversions constrain anomalies in terrestrial ecosystems? *Atmospheric Chemistry and Physics*, 19(20), 13,017–13,035. <https://doi.org/10.5194/acp-19-13017-2019>

Byrne, B., Jones, D. B. A., Strong, K., Zeng, Z. C., Deng, F., & Liu, J. (2017). Sensitivity of CO₂ surface flux constraints to observational coverage. *Journal of Geophysical Research: Atmosphere*, 112, 6672–6694. <https://doi.org/10.1002/2016JD026164>

Byrne, B., Wunch, D., Jones, D., Strong, K., Deng, F., Baker, I., et al. (2018). Evaluating GPP and respiration estimates over northern midlatitude ecosystems using solar-induced fluorescence and atmospheric CO₂ measurements. *Journal of Geophysical Research: Biogeosciences*, 123, 2976–2997. <https://doi.org/10.1029/2018JG004472>

Chatterjee, A., Gierach, M., Sutton, A., Feely, R., Crisp, D., Eldering, A., & Schimel, D. (2017). Influence of El Niño on atmospheric CO₂ over the tropical Pacific Ocean: Findings from NASAs OCO-2 mission. *Science*, 358, 6360. <https://doi.org/10.1126/science.aam5776>

Chevallier, F., Bréon, F. M., & Rayner, P. J. (2007). Contribution of the Orbiting Carbon Observatory to the estimation of CO₂ sources and sinks: Theoretical study in a variational data assimilation framework. *Journal of Geophysical Research*, 112, D09307. <https://doi.org/10.1029/2006JD007375>

Chevallier, F., Deutscher, N. M., Conway, T., Ciais, P., Ciattaglia, L., & Dohe, S. (2011). Global CO₂ fluxes inferred from surface air-sample measurements and from TCCON retrievals of the CO₂ total column. *Geophysical Research Letters*, 38, 24. <https://doi.org/10.1029/2011GL049899>

Chevallier, F., Remaud, M., O'Dell, C. W., Baker, D., Peylin, P., & Cozic, A. (2019). Objective evaluation of surface- and satellite-driven carbon dioxide atmospheric inversions. *Atmospheric Chemistry and Physics*, 19(22), 14,233–14,251. <https://doi.org/10.5194/acp-19-14233-2019>

Chevallier, F., Palmer, P. I., Feng, L., Boesch, H., O'Dell, C. W., & Bousquet, P. (2014). The Orbiting Carbon Observatory (OCO) mission. *Advances in Space Research*, 34(4), 700–709. <https://doi.org/10.1016/j.asr.2003.08.062>

- Cooperative global atmospheric data integration project (2018). Multi-laboratory compilation of atmospheric carbon dioxide data for the period 1957-2017; obspack_CO2_1_GLOBALVIEWplus_v4.1_2018_10_29; NOAA Earth System Research Laboratory, Global Monitoring Division. <https://doi.org/10.25925/20181026>
- Collatz, G. J., Menemenlis, D., Ott, L., Pawson, S., Jones, D. B. A., & Nassar, R. (2014). Carbon monitoring system flux estimation and attribution: impact of ACOS-GOSAT XCO₂ sampling on the inference of terrestrial biospheric sources and sinks. *Tellus B*, *66*(1), 22486. <https://doi.org/10.3402/tellusb.v66.22486>
- Crisp, D., Atlas, R., Breon, F., Brown, L., Burrows, J., & Ciais, P. (2004). The Orbiting Carbon Observatory (OCO) mission. *Advances in Space Research*, *34*(4), 700–709. <https://doi.org/10.1016/j.asr.2003.08.062>
- Crisp, D., Fisher, B. M., O'Dell, C., Frankenberg, C., Basilio, R., Bösch, H., & Yung, Y. L. (2012). The ACOS CO₂ retrieval algorithm—Part II: Global XCO₂ data characterization. *Atmospheric Measurement Techniques*, *5*(4), 687–707. <https://doi.org/10.5194/amt-5-687-2012>
- Crowell, S., Baker, D., Schuh, A., Basu, S., Jacobson, A. R., Chevallier, F., & Jones, D. B. A. (2019). The 2015–2016 carbon cycle as seen from OCO-2 and the global in situ network. *Atmospheric Chemistry and Physics*, *19*(15), 9797–9831. <https://doi.org/10.5194/acp-19-9797-2019>
- De Mazire, M., Sha, M. K., Desmet, F., Hermans, C., Scolas, F., Kumps, N., & Cammas, J. P. (2017). TCCON data from Reunion Island (RE), Release GGG2014.R1. CaltechDATA. Retrieved from <https://data.caltech.edu/records/322> doi: 10.14291/tcon.ggg2014.reunion01.r1.
- Diallo, M., Legras, B., Ray, E., Engel, A., & Añel, J. A. (2017). Global distribution of CO₂ in the upper troposphere and stratosphere. *Atmospheric Chemistry and Physics*, *17*(6), 3861–3878. <https://doi.org/10.5194/acp-17-3861-2017>
- Dorigo, W., Wagner, W., Albergel, C., Albrecht, F., Balsamo, G., Brocca, L., et al. (2017). ESA CCI Soil Moisture for improved Earth system understanding: State-of-the art and future directions. *Remote Sensing of Environment*, *203*, 185–215. <https://doi.org/10.1016/j.rse.2017.07.001>
- Dutkiewicz, S., Follows, M. J., & Bragg, J. G. (2009). Modeling the coupling of ocean ecology and biogeochemistry. *Global Biogeochemical Cycles*, *23*, 4. <https://doi.org/10.1029/2008GB003405>
- Eldering, A., O'Dell, C. W., Wennberg, P. O., Crisp, D., Gunson, M. R., Viatte, C., & Yoshimizu, J. (2017). The Orbiting Carbon Observatory-2: first 18 months of science data products. *Atmospheric Measurement Techniques*, *10*(2), 549–563. <https://doi.org/10.5194/amt-10-549-2017>
- Feist, D. G., Arnold, S. G., John, N., & Geibel, M. C. (2017). TCCON data from Ascension Island (SH), Release GGG2014.R0 CaltechDATA. Retrieved from <https://data.caltech.edu/records/210> doi:10.14291/tcon.ggg2014.ascension01.r0/1149285.
- Fischer, M. L., Parazoo, N., Brophy, K., Cui, X., Jeong, S., Liu, J., et al. (2017). Simulating estimation of California fossil fuel and biosphere carbon dioxide exchanges combining in situ tower and satellite column observations. *Journal of Geophysical Research: Atmosphere*, *122*, 3653–3671. <https://doi.org/10.1002/2016JD025617>
- Frankenberg, C., Kulawik, S. S., Wofsy, S. C., Chevallier, F., Daube, B., Kort, E. A., & Osterman, G. (2016). Using airborne HIAPER Pole-to-Pole Observations (HIPPO) to evaluate model and remote sensing estimates of atmospheric carbon dioxide. *Atmospheric Chemistry and Physics*, *16*(12), 7867–7878. <https://doi.org/10.5194/acp-16-7867-2016>
- Gelaro, R., McCarty, W., Suárez, M. J., Todling, R., Molod, A., Takacs, L., et al. (2017). The Modern-Era Retrospective analysis for Research and Applications, version 2 (MERRA-2). *Journal of Climate*, *30*(14), 5419–5454. <https://doi.org/10.1175/JCLI-D-16-0758.1>
- Griffith, D. W., Deutscher, N. M., Velasco, V. A., Wennberg, P. O., Yavin, Y., Keppel-Aleks, G., & Bryant, G. W. (2017). TCCON data from Darwin (AU), Release GGG2014.R0. CaltechDATA. Retrieved from <https://data.caltech.edu/records/269> doi: 10.14291/tcon.ggg2014.darwin01.r0/1149290.
- Griffith, D. W., Velasco, V. A., Deutscher, N. M., Paton-Walsh, C., Jones, N. B., Wilson, S. R., & Riggenbach, M. O. (2017). TCCON data from Wollongong (AU), Release GGG2014.R0. CaltechDATA. Retrieved from <https://data.caltech.edu/records/269> doi: 10.14291/tcon.ggg2014.darwin01.r0/1149290.
- Gruber, A., Dorigo, W. A., Crow, W., & Wagner, W. (2017). Triple collocation-based merging of satellite soil moisture retrievals. *IEEE Transactions on Geoscience and Remote Sensing*, *55*(12), 6780–6792. <https://doi.org/10.1109/TGRS.2017.2734070>
- Gurney, K. R., Baker, D., Rayner, P., & Denning, S. (2008). Interannual variations in continental-scale net carbon exchange and sensitivity to observing networks estimated from atmospheric CO₂ inversions for the period 1980 to 2005. *Global Biogeochemical Cycles*, *22*, 3. <https://doi.org/10.1029/2007GB003082>
- Houweling, S., Baker, D., Basu, S., Boesch, H., Butz, A., Chevallier, F., et al. (2015). An intercomparison of inverse models for estimating sources and sinks of CO₂ using GOSAT measurements. *Journal of Geophysical Research: Atmosphere*, *120*, 5253–5266. <https://doi.org/10.1002/2014JD022962>
- Huntzinger, D., Michalak, A., Schwalm, C., Ciais, P., King, A., Fang, Y., et al. (2017). Uncertainty in the response of terrestrial carbon sink to environmental drivers undermines carbon-climate feedback predictions. *Scientific Reports*, *7*, 4765. <https://doi.org/10.1038/s41598-017-03818-2>
- ICOS RI (2019). ICOS atmospheric greenhouse gas mole fractions of CO₂, CH₄, CO, ¹⁴CO₂ and meteorological observations September 2015 - April 2019 for 19 stations (49 vertical levels), final quality controlled Level 2 data (version 1.0). ICOS ERIC - Carbon Portal. <https://doi.org/10.18160/CE2R-CC91>
- Iraci, L. T., Podolske, J. R., Hillyard, P. W., Roehl, C., Wennberg, P. O., Blavier, J. F., & Boyden, H. (2017). TCCON data from Edwards (US), Release GGG2014.R1. CaltechDATA. Retrieved from <https://data.caltech.edu/records/270> doi: 10.14291/tcon.ggg2014.edwards01.r1/1255068.
- Jung, M., Reichstein, M., Schwalm, C. R., Huntingford, C., Sitch, S., Ahlström, A., et al. (2017). Compensatory water effects link yearly global land CO₂ sink changes to temperature. *Nature*, *541*(7638), 516–520.
- Keeling, C. D. (1960). The concentration and isotopic abundances of carbon dioxide in the atmosphere. *Tellus*, *12*(2), 200–203. <https://doi.org/10.1111/j.2153-3490.1960.tb01300.x>
- Keeling, C. D., Chin, J., & Whorf, T. (1996). Increased activity of northern vegetation inferred from atmospheric CO₂ measurements. *Nature*, *382*, 146–149.
- Kiel, M., O'Dell, C. W., Fisher, B., Eldering, A., Nassar, R., MacDonald, C. G., & Wennberg, P. O. (2019). How bias correction goes wrong: Measurement of XCO₂ affected by erroneous surface pressure estimates. *Atmospheric Measurement Techniques*, *12*, 4. <https://doi.org/10.5194/amt-12-2241-2019>
- Liu, J., & Bowman, K. (2016). A method for independent validation of surface fluxes from atmospheric inversion: Application to CO₂. *Geophysical Research Letters*, *43*, 3502–3508. <https://doi.org/10.1002/2016GL067828>
- Liu, J., Bowman, K., Parazoo, N. C., Bloom, A. A., Wunch, D., Jiang, Z., & Schimel, D. (2018). Detecting drought impact on terrestrial biosphere carbon fluxes over contiguous US with satellite observations. *Environmental Research Letters*, *13*(9), 95,003. <https://doi.org/10.1088/1748-9326/aad5ef>

- Liu, J., Bowman, K. W., Schimel, D. S., Parazoo, N. C., Jiang, Z., Lee, M., & Eldering, A. (2017). Contrasting carbon cycle responses of the tropical continents to the 2015–2016 El Niño. *Science*, 358, 6360. <https://doi.org/10.1126/science.aam5690>
- Liu, Y. Y., Dorigo, W. A., Parinussa, R., de Jeu, R. A., Wagner, W., McCabe, M. F., & Van Dijk, A. (2012). Trend-preserving blending of passive and active microwave soil moisture retrievals. *Remote Sensing Environment*, 123, 280–297. <https://doi.org/10.1016/j.rse.2012.03.014>
- Liu, Y. Y., Parinussa, R., Dorigo, W. A., De Jeu, R. A., Wagner, W., Van Dijk, A., & Evans, J. (2011). Developing an improved soil moisture dataset by blending passive and active microwave satellite-based retrievals. *Hydrology and Earth System Sciences*, 15(2), 425–436. <https://doi.org/10.5194/hess-15-425-2011>
- Machida, T., Matsueda, H., Sawa, Y., Nakagawa, Y., Hirotsu, K., Kondo, N., & Ogawa, T. (2008). Worldwide measurements of atmospheric CO₂ and other trace gas species using commercial airlines. *Journal of Atmospheric and Oceanic Technology*, 25(10), 1744–1754. <https://doi.org/10.1175/2008JTECHA1082.1>
- Machida, T., Matsueda, H., Sawa, Y., & Niwa, Y. (2018). Atmospheric CO₂ mole fraction data of CONTRAIL-CME, Ver.2017.1.0, Center for Global Environmental Research, NIES (Reference date: 2018/11/28). <https://doi.org/10.17595/20180208.001>
- Maksyutov, S., Takagi, H., Valsala, V. K., Saito, M., Oda, T., Saeki, T., & Yokota, T. (2013). Regional CO₂ flux estimates for 2009–2010 based on GOSAT and ground-based CO₂ observations. *Atmospheric Chemistry and Physics*, 13(18), 9351–9373. <https://doi.org/10.5194/acp-13-9351-2013>
- Masarie, K., Peters, W., Jacobson, A., & Tans, P. (2014). ObsPack: a framework for the preparation, delivery, and attribution of atmospheric greenhouse gas measurements. *Earth System Science Data*, 6(2), 375–384.
- Menemenlis, D., Campin, J. M., Heimbach, P., Hill, C., Lee, T., Nguyen, A., & Zhang, H. (2008). ECCO₂: High resolution global ocean and sea ice data synthesis. *Mercator Ocean Quarterly Newsletter*, 31(October), 13–21.
- Miller, S. M., & Michalak, A. M. (2020). The impact of improved satellite retrievals on estimates of biospheric carbon balance. *Atmospheric Chemistry and Physics*, 20, 323–331. <https://doi.org/10.5194/acp-20-323-2020>
- Morino, I., Yokozeki, N., Matsuzaki, T., & Horikawa, M. (2017). TCCON data from Rikubetsu (JP), Release GGG2014.R2. CaltechDATA Retrieved from <https://data.caltech.edu/records/957> doi:10.14291/tcon.ggg2014.rikubetsu01.r2.
- Nassar, R., Jones, D., Kulawik, S., Worden, J., Bowman, K., Andres, R. J., et al. (2011). Inverse modeling of CO₂ sources and sinks using satellite observations of CO₂ from TES and surface flask measurements. *Atmospheric Chemistry and Physics*, 11(12), 6029–6047. <https://doi.org/10.5194/acp-11-6029-2011>
- Nassar, R., Napier-Linton, L., Gurney, K. R., Andres, R. J., Oda, T., Vogel, F. R., & Deng, F. (2013). Improving the temporal and spatial distribution of CO₂ emissions from global fossil fuel emission data sets. *Journal of Geophysical Research: Atmosphere*, 118, 917–933. <https://doi.org/10.1029/2012JD018196>
- Nassar, R., Sioris, C. E., Jones, D., & McConnell, J. C. (2014). Satellite observations of CO₂ from a highly elliptical orbit for studies of the Arctic and boreal carbon cycle. *Journal of Geophysical Research: Atmosphere*, 119, 2654–2673. <https://doi.org/10.1002/2013JD020337>
- Nelson, R. R., & O'Dell, C. W. (2019). The impact of improved aerosol priors on near-infrared measurements of carbon dioxide. *Atmospheric Measurement Techniques*, 12(3), 1495–1512. <https://doi.org/10.5194/amt-12-1495-2019>
- O'Dell, C. W., Connor, B., Bösch, H., O'Brien, D., Frankenberg, C., Castano, R., & Wunch, D. (2012). The ACOS CO₂ retrieval algorithm—Part 1: Description and validation against synthetic observations. *Atmospheric Measurement Techniques*, 5(1), 99–121. <https://doi.org/10.5194/amt-5-99-2012>
- O'Dell, C. W., Eldering, A., Wennberg, P. O., Crisp, D., Gunson, M. R., Fisher, B., & Velasco, V. A. (2018). Improved retrievals of carbon dioxide from Orbiting Carbon Observatory-2 with the version 8 ACOS algorithm. *Atmospheric Measurement Techniques*, 11(12), 6539–6576. <https://doi.org/10.5194/amt-11-6539-2018>
- Oda, T., & Maksyutov, S. (2011). A very high-resolution (1km×1km) global fossil fuel CO₂ emission inventory derived using a point source database and satellite observations of nighttime lights. *Atmospheric Chemistry and Physics*, 11(2). <https://doi.org/10.5194/acp-11-543-2011>
- Oda, T., Maksyutov, S., & Andres, R. J. (2018). The open-source data inventory for anthropogenic CO₂, version 2016 (ODIAC2016): A global monthly fossil fuel CO₂ gridded emissions data product for tracer transport simulations and surface flux inversions. *Earth Systems Science Data*, 10(1), 87–107. <https://doi.org/10.5194/essd-10-87-2018>
- Olsen, S. C., & Randerson, J. T. (2004). Differences between surface and column atmospheric CO₂ and implications for carbon cycle research. *Journal of Geophysical Research*, 109, D02301. <https://doi.org/10.1029/2003JD003968>
- Parazoo, N. C., Denning, A. S., Kawa, S. R., Pawson, S., & Lokupitiya, R. (2012). 14. *Atmospheric Chemistry and Physics*, 12, 6405–6416. <https://doi.org/10.5194/acp-12-6405-2012>
- Peylin, P., Breon, F. M., Serrar, S., Tiwari, Y., Chedin, A., Gloor, M., & Ciais, P. (2007). Evaluation of Television Infrared Observation Satellite (TIROS-N) Operational Vertical Sounder (TOVS) spaceborne CO₂ estimates using model simulations and aircraft data. *Journal of Geophysical Research*, 112, D9. <https://doi.org/10.1029/2005JD007018>
- Philip, S., Johnson, M. S., Potter, C., Genovesse, V., Baker, D. F., Haynes, K. D., & Poulter, B. (2019). Prior biosphere model impact on global terrestrial CO₂ fluxes estimated from OCO-2 retrievals. *Atmospheric Chemistry and Physics*, 19(20), 13,267–13,287. <https://doi.org/10.5194/acp-19-13267-2019>
- Pickett-Heaps, C., Rayner, P., Law, R., Ciais, P., Patra, P., Bousquet, P., et al. (2011). Atmospheric CO₂ inversion validation using vertical profile measurements: Analysis of four independent inversion models. *Journal of Geophysical Research*, 116, D12305. <https://doi.org/10.1029/2010JD014887>
- Polavarapu, S. M., Deng, F., Byrne, B., Jones, D. B. A., & Neish, M. (2018). A comparison of posterior atmospheric CO₂ adjustments obtained from in situ and GOSAT constrained flux inversions. *Atmospheric Chemistry and Physics*, 18(16), 12,011–12,044. <https://doi.org/10.5194/acp-18-12011-2018>
- Randerson, J. T., Thompson, M. V., Malmstrom, C. M., Field, C. B., & Fung, I. Y. (1996). Substrate limitations for heterotrophs: Implications for models that estimate the seasonal cycle of atmospheric CO₂. *Global Biogeochemical Cycles*, 10(4), 585–602. <https://doi.org/10.1029/96GB01981>
- Randerson, J. T., Van Der Werf, G., Giglio, L., Collatz, G., & Kasibhatla, P. (2018). Global Fire Emissions Database, Version 4.1 (GFEDv4) ORNL DAAC. <https://doi.org/10.3334/ORNLDAAC/1293>
- Reichle, R. H., Draper, C. S., Liu, Q., Girotto, M., Mahanama, S. P., Koster, R. D., & De Lannoy, G. J. (2017). Assessment of MERRA-2 land surface hydrology estimates. *Journal of Climate*, 30(8), 2937–2960. <https://doi.org/10.1175/JCLI-D-16-0720.1>
- Reichle, R. H., Koster, R. D., De Lannoy, G. J., Forman, B. A., Liu, Q., Mahanama, S. P., & Touré, A. (2011). Assessment and enhancement of MERRA land surface hydrology estimates. *Journal of Climate*, 24(24), 6322–6338. <https://doi.org/10.1175/JCLI-D-10-05033.1>

- Reuter, M., Buchwitz, M., Hilker, M., Heymann, J., Schneising, O., Pillai, D., et al. (2014). Satellite-inferred European carbon sink larger than expected. *Atmospheric Chemistry and Physics*, *14*(24), 13,739–13,753. <https://doi.org/10.5194/acp-14-13739-2014>
- Rödenbeck, C., Houweling, S., Gloor, M., & Heimann, M. (2003). CO₂ flux history 1982–2001 inferred from atmospheric data using a global inversion of atmospheric transport. *Atmospheric Chemistry and Physics*, *3*(6), 1919–1964. <https://doi.org/10.5194/acp-3-1919-2003>
- Saeki, T., Maksyutov, S., Saito, M., Valsala, V., Oda, T., Andres, R. J., et al. (2013). Inverse modeling of CO₂ fluxes using GOSAT data and multi-year ground-based observations. *SOLA*, *9*, 45–50. <https://doi.org/10.2151/sola.2013-011>
- Sasakawa, M., Machida, T., Tsuda, N., Arshinov, M., Davydov, D., Fofonov, A., & Krasnov, O. (2013). Aircraft and tower measurements of CO₂ concentration in the planetary boundary layer and the lower free troposphere over southern taiga in West Siberia: Long-term records from 2002 to 2011. *Journal of Geophysical Research: Atmosphere*, *118*, 9489–9498. <https://doi.org/10.1002/jgrd.50755>
- Sasakawa, M., Shimoyama, K., Machida, T., Tsuda, N., Suto, H., Arshinov, M., et al. (2010). Continuous measurements of methane from a tower network over Siberia. *Tellus B*, *62*(5), 403–416. <https://doi.org/10.1111/j.1600-0889.2010.00494.x>
- Schuh, A. E., Jacobson, A. R., Basu, S., Weir, B., Baker, D., Bowman, K., et al. (2019). Quantifying the impact of atmospheric transport uncertainty on CO₂ surface flux estimates. *Global Biogeochemical Cycles*, *33*, 84–500. <https://doi.org/10.1029/2018GB006086>
- Sellers, P., Randall, D., Collatz, G., Berry, J., Field, C., Dazlich, D., & Bounoua, L. (1996). A revised land surface parameterization (SiB2) for atmospheric GCMs. Part I: Model formulation. *Journal of Climate*, *9*(4), 676–705. [https://doi.org/10.1175/1520-0442\(1996\)009<0676:ARLSPF>2.0.CO;2](https://doi.org/10.1175/1520-0442(1996)009<0676:ARLSPF>2.0.CO;2)
- Sellers, P. J., Tucker, C. J., Collatz, G. J., Los, S. O., Justice, C. O., Dazlich, D. A., & Randall, D. A. (1996). A revised land surface parameterization (SiB2) for atmospheric GCMs. Part II: The generation of global fields of terrestrial biophysical parameters from satellite data. *Journal of Climate*, *9*(4), 706–737. [https://doi.org/10.1175/1520-0442\(1996\)009<0706:ARLSPF>2.0.CO;2](https://doi.org/10.1175/1520-0442(1996)009<0706:ARLSPF>2.0.CO;2)
- Stephens, B. B., Gurney, K. R., Tans, P. P., Sweeney, C., Peters, W., Bruhwiler, L., et al. (2007). Weak northern and strong tropical land carbon uptake from vertical profiles of atmospheric CO₂. *Science*, *316*(5832), 1732–1735. <https://doi.org/10.1126/science.1137004>
- Strong, K., Roche, S., Franklin, J. E., Mendonca, J., Lutsch, E., Weaver, D., & Lindenmaier, R. (2017). TCCON data from Eureka (CA), Release GGG2014.R2. CaltechDATA. Retrieved from <https://data.caltech.edu/records/970doi:10.14291/tcon.ggg2014.eureka01.r2>
- Sweeney, C., Karion, A., Wolter, S., Newberger, T., Guenther, D., Higgs, J. A., et al. (2015). Seasonal climatology of CO₂ across North America from aircraft measurements in the NOAA/ESRL Global Greenhouse Gas Reference Network. *Journal of Geophysical Research: Atmospheres*, *120*, 5155–5190. <https://doi.org/10.1002/2014JD022591>
- Tans, P. P., Conway, T. J., & Nakazawa, T. (1989). Latitudinal distribution of the sources and sinks of atmospheric carbon dioxide derived from surface observations and an atmospheric transport model. *Journal of Geophysical Research: Atmospheres*, *94*, 5151–5172. <https://doi.org/10.1029/JD094iD04>
- Tramontana, G., Jung, M., Schwalm, C. R., Ichii, K., Camps-Valls, G., Ráduly, B., & Papale, D. (2016). Predicting carbon dioxide and energy fluxes across global FLUXNET sites with regression algorithms. *Biogeosciences*, *13*(14), 4291–4313. <https://doi.org/10.5194/bg-13-4291-2016>
- van der Werf, G. R., Randerson, J. T., Giglio, L., Collatz, G. J., Kasibhatla, P. S., & Arellano Jr, A. F. (2006). Interannual variability in global biomass burning emissions from 1997 to 2004. *Atmospheric Chemistry and Physics*, *6*(11), 3423–3441. <https://doi.org/10.5194/acp-6-3423-2006>
- Vidale, P., & Stöckli, R. (2005). Prognostic canopy air space solutions for land surface exchanges. *Theoretical and Applied Climatology*, *80*(2-4), 245–257. <https://doi.org/10.1007/s00704-004-0103-2>
- Wagner, W., Dorigo, W., de Jeu, R., Fernandez, D., Benveniste, J., Haas, E., & Ertl, M. (2012). Fusion of active and passive microwave observations to create an essential climate variable data record on soil moisture. *ISPRS Annals of the Photogrammetry, Remote Sensing and Spatial Information Sciences (ISPRS Annals)*, *7*, 315–321.
- Wang, J. S., Kawa, S. R., Collatz, G. J., Sasakawa, M., Gatti, L. V., Machida, T., & Manyin, M. E. (2018). A global synthesis inversion analysis of recent variability in CO₂ fluxes using GOSAT and in situ observations. *Atmospheric Chemistry and Physics*, *18*(15), 11,097–11,124. <https://doi.org/10.5194/acp-18-11097-2018>
- Warneke, T., Messerschmidt, J., Notholt, J., Weinzierl, C., Deutscher, N. M., Petri, C., & Grupe, P. (2017). TCCON data from Orlans (FR), Release GGG2014.R0. CaltechDATA. doi:10.14291/tcon.ggg2014.orleans01.r0/1149276.
- Wennberg, P. O., Roehl, C. M., Wunch, D., Toon, G. C., Blavier, J. F., Washenfelder, R., & Ayers, J. (2017). TCCON data from Park Falls (US), Release GGG2014.R1. CaltechDATA. Retrieved from <https://data.caltech.edu/records/295doi:10.14291/tcon.ggg2014.park-falls01.r1>
- Wennberg, P. O., Wunch, D., Roehl, C. M., Blavier, J. F., Toon, G. C., & Allen, N. T. (2017). TCCON data from Lamont (US), Release GGG2014.R1. Caltech-DATA. Retrieved from <https://data.caltech.edu/records/279doi:10.14291/tcon.ggg2014.lamont01.r1/1255070>
- Wofsy, S. C. (2011). HIAPER Pole-to-Pole Observations (HIPPO): Fine-grained, global-scale measurements of climatically important atmospheric gases and aerosols. *Philosophical Transactions of the Royal Society*, *369*(1943), 2073–2086. <https://doi.org/10.1098/rsta.2010.0313>
- Wunch, D., Toon, G. C., Blavier, J. F. L., Washenfelder, R. A., Notholt, J., Connor, B. J., & Wennberg, P. O. (2011). The Total Carbon Column Observing Network. *Philosophical Transactions of the Royal Society A*, *369*(1943), 2087–2112. <https://doi.org/10.1098/rsta.2010.0240>
- Wunch, D., Toon, G. C., Wennberg, P. O., Wofsy, S. C., Stephens, B. B., Fischer, M. L., & Zondlo, M. A. (2010). Calibration of the Total Carbon Column Observing Network using aircraft profile data. *Atmospheric Measurement Techniques*, *3*(5), 1351–1362. <https://doi.org/10.5194/amt-3-1351-2010>
- Yokota, T., Yoshida, Y., Eguchi, N., Ota, Y., Tanaka, T., Watanabe, H., & Maksyutov, S. (2009). Global concentrations of CO₂ and CH₄ retrieved from GOSAT: First preliminary results. *Sola*, *5*, 160–163. <https://doi.org/10.2151/sola.2009-041>
- Yoshida, Y., Kikuchi, N., Morino, I., Uchino, O., Oshchepkov, S., Bril, A., & Yokota, T. (2013). Improvement of the retrieval algorithm for GOSAT SWIR XCO₂ and XCH₄ and their validation using TCCON data. *Atmospheric Measurement Techniques*, *6*(6), 1533–1547. <https://doi.org/10.5194/amt-6-1533-2013>
- Yu, K., Keller, C. A., Jacob, D. J., Molod, A. M., Eastham, S. D., & Long, M. S. (2018). Errors and improvements in the use of archived meteorological data for chemical transport modeling: An analysis using GEOS-Chem v11-01 driven by GEOS-5 meteorology. *Geoscientific Model Development*, *11*(1), 305–319. <https://doi.org/10.5194/gmd-11-305-2018>